

SECTION

I

---

*THREE-DIMENSIONAL  
VOLUMETRIC DNG  
METAMATERIALS*



# INTRODUCTION, HISTORY, AND SELECTED TOPICS IN FUNDAMENTAL THEORIES OF METAMATERIALS

*Richard W. Ziolkowski and Nader Engheta*

## 1.1 INTRODUCTION

To the best of our knowledge, the first attempt to explore the concept of “artificial” materials appears to trace back to the late part of the nineteenth century when in 1898 Jagadis Chunder Bose conducted the first microwave experiment on twisted structures—geometries that were essentially artificial chiral elements by today’s terminology [1]. In 1914, Lindman worked on “artificial” chiral media by embedding many randomly oriented small wire helices in a host medium [2]. In 1948, Kock [3] made lightweight microwave lenses by arranging conducting spheres, disks, and strips periodically and effectively tailoring the effective refractive index of the artificial media. Since then, artificial complex materials have been the subject of research for many investigators worldwide. In recent years new concepts in synthesis and novel fabrication techniques have allowed the construction of structures and composite materials that mimic known material responses or that qualitatively have new, physically realizable response functions that do not occur or may not be readily available in nature. These metamaterials can in principle be synthesized by embedding various constituents/inclusions with novel geometric shapes and forms in some host media (Fig. 1.1). Various types of electromagnetic composite media, such as double-negative (DNG) materials, chiral materials, omega media, wire media, bianisotropic media, linear and nonlinear media, and local and nonlocal media, to name a few, have been studied by various research groups worldwide.

As is well known, in particulate composite media, electromagnetic waves interact with the inclusions, inducing electric and magnetic moments, which in turn affect the macroscopic effective permittivity and permeability of the bulk composite “medium.” Since metamaterials can be synthesized by embedding artificially fabricated inclusions in a specified host medium or on a host surface, this provides the designer with a large collection of independent parameters (or

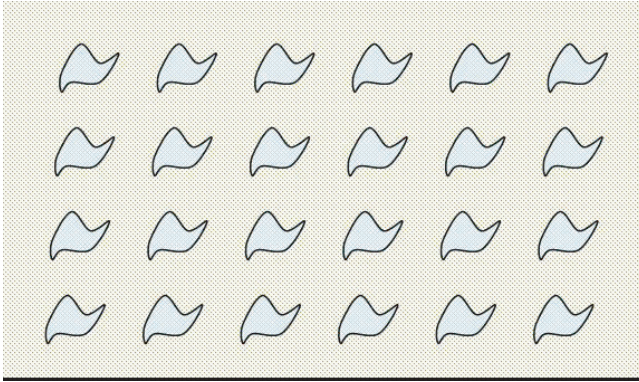


**Figure 1.1** Generic sketch of a volumetric metamaterial synthesized by embedding various inclusions in a host medium.

degrees of freedom)—such as the properties of the host materials; the size, shape, and composition of the inclusions; and the density, arrangement, and alignment of these inclusions—to work with in order to *engineer* a metamaterial with specific electromagnetic response functions not found in each of the individual constituents. All of these design parameters can play a key role in the final outcome of the synthesis process. Among these, the geometry (or shape) of the inclusions is one that can provide a variety of new possibilities for metamaterials processing.

Recently, the idea of complex materials in which both the permittivity and the permeability possess negative real values at certain frequencies has received considerable attention. In 1967, Veselago theoretically investigated plane-wave propagation in a material whose permittivity and permeability were assumed to be simultaneously negative [4]. His theoretical study showed that for a monochromatic uniform plane wave in such a medium the direction of the Poynting vector is antiparallel to the direction of the phase velocity, contrary to the case of plane-wave propagation in conventional simple media. In recent years, Smith, Schultz, and their group constructed such a composite medium for the microwave regime and demonstrated experimentally the presence of anomalous refraction in this medium [5, 6].

For metamaterials with negative permittivity and permeability, several names and terminologies have been suggested, such as “left-handed” media [4–10]; media with negative refractive index [4–7, 9]; “backward-wave media” (BW media) [11]; and “double-negative (DNG)” metamaterials [12], to name a few. Many research groups all over the world are now studying various aspects of this class of metamaterials, and several ideas and suggestions for future applications of these materials have been proposed.

It is well known that the response of a system to the presence of an electromagnetic field is determined to a large extent by the properties of the materials involved. We describe these properties by defining the macroscopic parameters permittivity  $\epsilon$  and permeability  $\mu$  of these materials. This allows for the classification of a medium as follows. A medium with both permittivity

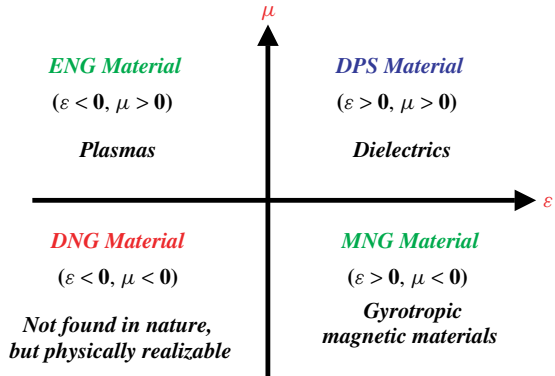


**Figure 1.2** Material classifications.

and permeability greater than zero ( $\epsilon > 0, \mu > 0$ ) will be designated a double-positive (DPS) medium. Most naturally occurring media (e.g., dielectrics) fall under this designation. A medium with permittivity less than zero and permeability greater than zero ( $\epsilon < 0, \mu > 0$ ) will be designated an epsilon-negative (ENG) medium. In certain frequency regimes many plasmas exhibit this characteristic. For example, noble metals (e.g., silver, gold) behave in this manner in the infrared (IR) and visible frequency domains. A medium with the permittivity greater than zero and permeability less than zero ( $\epsilon > 0, \mu < 0$ ) will be designated a mu-negative (MNG) medium. In certain frequency regimes some gyrotropic materials exhibit this characteristic. Artificial materials have been constructed that also have DPS, ENG, and MNG properties. A medium with both the permittivity and permeability less than zero ( $\epsilon < 0, \mu < 0$ ) will be designated a DNG medium. To date, this class of materials has only been demonstrated with artificial constructs. This medium classification can be graphically illustrated as shown in Figure 1.2.

While one often describes a material by some constant (frequency-independent) value of the permittivity and permeability, in reality all material properties are frequency dependent. There are several material models that have been constructed to describe the frequency response of materials. Because the magnetic field of an electromagnetic wave is smaller than its electric field by the wave impedance of the medium in which it is propagating, one generally focuses attention on how the electron motion in the presence of the nucleus and, hence, the basic dipole moment of this system are changed by the electric field. Understanding this behavior leads to a model of the electric susceptibility of the medium and, hence, its permittivity. On the other hand, there are many media for which the magnetic field response is dominant. One can generally describe the magnetic response of a material in a fashion completely dual to that of the electric field using the magnetic susceptibility and, hence, its permeability. While the magnetic dipoles physically arise from moments associated with current loops, they can be described mathematically by magnetic charge and current analogs of the electric cases.

One of the most well-known material models is the *Lorentz* model. It is derived by a description of the electron motion in terms of a driven, damped

harmonic oscillator. To simplify the discussion, we will assume that the charges are allowed to move in the same direction as the electric field. The Lorentz model then describes the temporal response of a component of the polarization field of the medium to the same component of the electric field as

$$\frac{d^2}{dt^2}P_i + \Gamma_L \frac{d}{dt}P_i + \omega_0^2 P_i = \varepsilon_0 \chi_L E_i \quad (1.1)$$

The first term on the left accounts for the acceleration of the charges, the second accounts for the damping mechanisms of the system with damping coefficient  $\Gamma_L$ , and the third accounts for the restoring forces with the characteristic frequency  $f_0 = \omega_0/2\pi$ . The driving term exhibits a coupling coefficient  $\chi_L$ . The response in the frequency domain, assuming the engineering  $\exp(+j\omega t)$  time dependence, is given by the expression

$$P_i(\omega) = \frac{\chi_L}{-\omega^2 + j\Gamma_L\omega + \omega_0^2} \varepsilon_0 E_i(\omega) \quad (1.2)$$

With small losses  $\Gamma_L/\omega_0 \ll 1$  the response is clearly resonant at the natural frequency  $f_0$ . The polarization and electric fields are related to the electric susceptibility as

$$\chi_{e,\text{Lorentz}}(\omega) = \frac{P_i(\omega)}{\varepsilon_0 E_i(\omega)} = \frac{\chi_L}{-\omega^2 + j\Gamma_L\omega + \omega_0^2} \quad (1.3)$$

The permittivity is then obtained immediately as  $\varepsilon_{\text{Lorentz}}(\omega) = \varepsilon_0[1 + \chi_{e,\text{Lorentz}}(\omega)]$ .

There are several well-known special cases of the Lorentz model. When the acceleration term is small in comparison to the others, one obtains the *Debye* model:

$$\Gamma_d \frac{d}{dt}P_i + \omega_0^2 P_i = \varepsilon_0 \chi_d E_i \quad \chi_{e,\text{Debye}}(\omega) = \frac{\chi_d}{j\Gamma_d\omega + \omega_0^2} \quad (1.4)$$

When the restoring force is negligible, one obtains the *Drude* model:

$$\frac{d^2}{dt^2}P_i + \Gamma_D \frac{d}{dt}P_i = \varepsilon_0 \chi_D E_i \quad \chi_{e,\text{Drude}}(\omega) = \frac{\chi_D}{-\omega^2 + j\Gamma_D\omega} \quad (1.5)$$

where the coupling coefficient is generally represented by the plasma frequency  $\chi_D = \omega_p^2$ . In all of these models, the high-frequency limit reduces the permittivity to that of free space.

Assuming that the coupling coefficient is positive, then only the Lorentz and the Drude models can produce negative permittivities. Because the Lorentz model is resonant, the real part of the susceptibility and, hence, that of the permittivity become negative in a narrow frequency region immediately above the resonance. On the other hand, the Drude model can yield a negative real part of the permittivity over a wide spectral range, that is, for  $\omega < \sqrt{\omega_p^2 - \Gamma_D^2}$ .

Similar magnetic response models follow immediately. The corresponding magnetization field components  $M_i$  and the magnetic susceptibility  $\chi_m$  equations are obtained from the polarization and electric susceptibility expressions with the replacements  $E_i \rightarrow H_i$ ,  $P_i/\varepsilon_0 \rightarrow M_i$ . The permeability is given as  $\mu(\omega) = \mu_0[1 + \chi_m(\omega)]$ .

Metamaterials have necessitated the introduction of generalizations of these models. For instance, the most general second-order model that has been introduced for metamaterial studies is the two-time-derivative Lorentz metamaterial (2TDLM) model [13–15]:

$$\begin{aligned} \frac{d^2}{dt^2}P_i + \Gamma_L \frac{d}{dt}P_i + \omega_0^2 P_i &= \varepsilon_0 \chi_\alpha \omega_p^2 E_i + \varepsilon_0 \chi_\beta \omega_p \frac{d}{dt}E_i + \varepsilon_0 \chi_\gamma \frac{d^2}{dt^2}E_i \\ \chi_{e,2TDLM}(\omega) &= \frac{\chi_\alpha \omega_p^2 + j \chi_\beta \omega_p \omega - \chi_\gamma \omega^2}{-\omega^2 + j \Gamma_L \omega + \omega_0^2} \end{aligned} \quad (1.6)$$

This 2TDLM model incorporates all the standard Lorentz model behaviors including the resonance behavior at  $\omega_0$  but allows for additional driving mechanisms that are important when considering time-varying phenomena. It satisfies a generalized Kramers–Krönig relation and is causal if  $\chi_\gamma > -1$ . It has the limiting behaviors  $\lim_{\omega \rightarrow 0} \chi_{e,2TDLM}(\omega) \rightarrow \chi_\alpha$  and  $\lim_{\omega \rightarrow \infty} \chi_{e,2TDLM}(\omega) \rightarrow \chi_\gamma$ . The high-frequency behavior has the peculiar property that if  $-1 < \chi_\gamma < 0$ , then  $0 < \lim_{\omega \rightarrow \infty} \varepsilon(\omega) < 1$ , which leads to the interesting but still controversial transvacuum-speed (TVS) effect [16, 17].

## 1.2 WAVE PARAMETERS IN DNG MEDIA

One must exercise some care with the definitions of the electromagnetic properties in a DNG medium. Ziolkowski and Heyman thoroughly analyzed this concept mathematically and have shown that in DNG media the refractive index can be negative [12]. In particular, in a DNG medium where  $\varepsilon < 0$  and  $\mu < 0$ , one should write for small losses:

$$\begin{aligned} \sqrt{\varepsilon} &= \sqrt{\varepsilon_r \varepsilon_0 - j \varepsilon''} \approx -j \left( |\varepsilon_r \varepsilon_0|^{1/2} + j \frac{\varepsilon''}{2|\varepsilon_r \varepsilon_0|^{1/2}} \right) \\ \sqrt{\mu} &= \sqrt{\mu_r \mu_0 - j \mu''} \approx -j \left( |\mu_r \mu_0|^{1/2} + j \frac{\mu''}{2|\mu_r \mu_0|^{1/2}} \right) \end{aligned} \quad (1.7)$$

accounting for the branch-cut choices. This leads to the following expressions for the wavenumber and the wave impedance, respectively:

$$\begin{aligned} k &= \omega \sqrt{\varepsilon} \sqrt{\mu} \approx -\frac{\omega}{c} |\varepsilon_r|^{1/2} |\mu_r|^{1/2} \left[ 1 + j \frac{1}{2} \left( \frac{\varepsilon''}{|\varepsilon_r| \varepsilon_0} + \frac{\mu''}{|\mu_r| \mu_0} \right) \right] \\ \eta &= \frac{\sqrt{\mu}}{\sqrt{\varepsilon}} \approx \eta_0 \frac{|\mu_r|^{1/2}}{|\varepsilon_r|^{1/2}} \left[ 1 + j \frac{1}{2} \left( \frac{\mu''}{|\mu_r| \mu_0} - \frac{\varepsilon''}{|\varepsilon_r| \varepsilon_0} \right) \right] \end{aligned} \quad (1.8)$$

where the speed of light  $c = 1/\sqrt{\varepsilon_0 \mu_0}$  and the free-space wave impedance  $\eta_0 = \sqrt{\mu_0/\varepsilon_0}$ . One sees that the index of refraction

$$\begin{aligned} n &= \frac{kc}{\omega} = \sqrt{\frac{\varepsilon}{\varepsilon_0}} \sqrt{\frac{\mu}{\mu_0}} = - \left[ \left( |\varepsilon_r| |\mu_r| - \frac{\varepsilon'' \mu''}{\varepsilon_0 \mu_0} \right) + j \left( \frac{\varepsilon'' |\mu_r|}{\varepsilon_0} + \frac{\mu'' |\varepsilon_r|}{\mu_0} \right) \right]^{1/2} \\ &\approx -|\varepsilon_r|^{1/2} |\mu_r|^{1/2} \left[ 1 + j \frac{1}{2} \left( \frac{\varepsilon''}{|\varepsilon_r| \varepsilon_0} + \frac{\mu''}{|\mu_r| \mu_0} \right) \right] \end{aligned} \quad (1.9)$$

has a negative real part. Its imaginary part is also negative corresponding to the passive nature of the DNG medium.

The index of refraction of a DNG metamaterial has been shown theoretically to be negative by several groups (e.g., [8, 12, 18]), and several experimental studies have been reported confirming this negative-index-of-refraction (NIR) property and applications derived from it, such as phase compensation and electrically small resonators [19], negative angles of refraction (e.g., [6, 19–24]), sub-wavelength waveguides with lateral dimension below diffraction limits [25–30], enhanced focusing (see [7, 31]), backward-wave antennas [32], Čerenkov radiation [33], photon tunneling [34, 35], and enhanced electrically small antennas [36]. These studies rely heavily on the concept that a continuous-wave (CW) excitation of a DNG medium leads to a NIR and, hence, to negative or compensated phase terms.

### 1.3 FDTD SIMULATIONS OF DNG MEDIA

In this chapter and in Chapter 2, we present several finite-difference time-domain (FDTD) simulation results for wave interactions with DNG media, in addition to analytical descriptions. Consequently, we briefly discuss some of the features of the FDTD simulator specific to the DNG structures. It should be emphasized that the use of this purely numerical simulation approach does not involve any choices in defining derived quantities to explain the wave physics, for example, no wave vector directions or wave speeds are stipulated a priori. In this manner, it has provided a useful approach to studying the wave physics associated with DNG metamaterials.

As in [12, 22, 23, 37], lossy Drude polarization and magnetization models are used to simulate the DNG medium; specifically the permittivity and permeability are described in the frequency domain as

$$\begin{aligned}\varepsilon(\omega) &= \varepsilon_0 \left( 1 - \frac{\omega_{pe}^2}{\omega(\omega - j\Gamma_e)} \right) \\ \mu(\omega) &= \mu_0 \left( 1 - \frac{\omega_{pm}^2}{\omega(\omega - j\Gamma_m)} \right)\end{aligned}\tag{1.10}$$

where  $\omega_{pe}$ ,  $\omega_{pm}$  and  $\Gamma_e$ ,  $\Gamma_m$  denote the corresponding plasma and damping frequencies, respectively. These models are implemented into the FDTD scheme by introducing the associated electric and magnetic current densities and the equations that govern their temporal behavior.

$$\begin{aligned}J_{i,\text{Drude}} &= \frac{d}{dt} P_i \\ \frac{d}{dt} J_{i,\text{Drude}} + \Gamma_e J_{i,\text{Drude}} &= \varepsilon_0 \omega_p^2 E_i \\ K_{i,\text{Drude}} &= \frac{d}{dt} M_i \\ \frac{d}{dt} K_{i,\text{Drude}} + \Gamma_m K_{i,\text{Drude}} &= \omega_p^2 H_i\end{aligned}\tag{1.11}$$

The choices of the space and time locations of the discretized electric and magnetic currents, as well as the polarization and magnetization fields, are made self-consistently following the conventional FDTD method [38]. The simulation space is truncated with a metamaterial-based absorbing boundary condition [15,39]. The FDTD cell size in all of the cases presented here was  $\lambda_0/100$  to minimize the impact of any numerical dispersion on the results.

Although in some of the analytical and numerical studies, as well as experiments, considered by other groups (e.g., [5, 6, 18, 40–43]) the Lorentz model and its derivatives have been used, here the Drude model is preferred for the FDTD simulations for both the permeability and permittivity functions because it provides a much wider bandwidth over which the negative values of the permittivity and permeability can be obtained. This choice is only for numerical convenience and it does not alter any conclusions derived from such simulations; that is, the negative refraction is observed in either choice. However, choosing the Drude model for the FDTD simulation also implies that the overall simulation time can be significantly shorter, particularly for low-loss media. In other words, the FDTD simulation will take longer to reach a steady state in the corresponding Lorentz model because the resonance region where the permittivity and permeability acquire their negative values would be very narrow in this model.

## 1.4 CAUSALITY IN DNG MEDIA

As for the causality of signal propagation in a DNG medium, we note that if one totally ignores the temporal dispersion in a DNG medium and considers carefully the ramifications of a homogeneous, *nondispersive* DNG medium and the resulting NIR, one will immediately encounter a causality paradox in the time domain, that is, a nondispersive DNG medium is noncausal. However, a resolution of this issue was uncovered in [44] by taking the dispersion into account in a time-domain study of wave propagation in DNG media. The causality of waves propagating in a *dispersive* DNG metamaterial was investigated both analytically and numerically using the one-dimensional (1D) electromagnetic plane-wave radiation from a current sheet source in a dispersive DNG medium. A lossy Drude model of the DNG medium was used, and the solution was generated numerically with the FDTD method. The basic 1D geometry is shown in Figure 1.3. The signal direction of propagation (D.O.P.) is from left to right.

A causal result would show that the signal arrives at point 1 before point 2; an NIR result would then show that the peaks of the signals received at point 2 occur before those at point 1 once steady state is reached. The FDTD predicted results, shown in Figure 1.4, confirm this behavior.

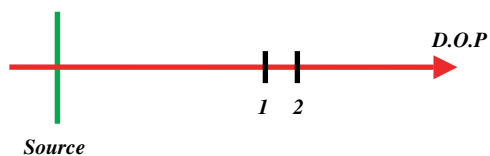


**Figure 1.3** One-dimensional FDTD simulation region.

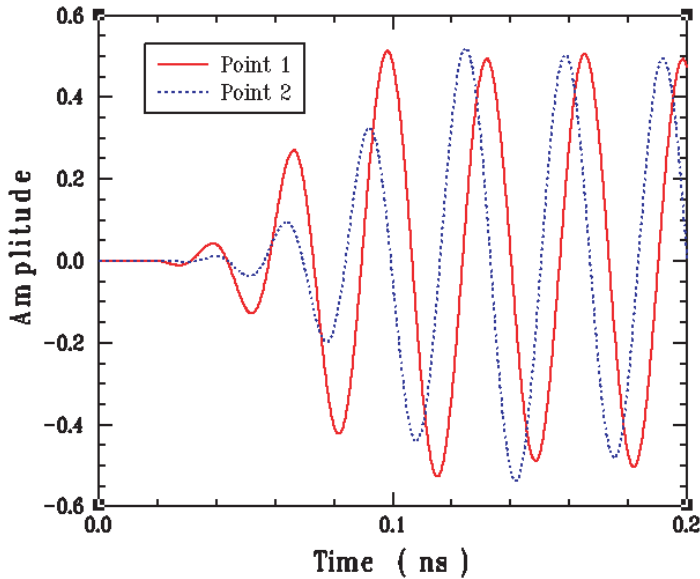


**Figure 1.4** Time-domain electric fields predicted by the FDTD simulator at points 1 and 2 shown in Figure 1.3. From [44]. Copyright © 2003 by the American Physical Society.

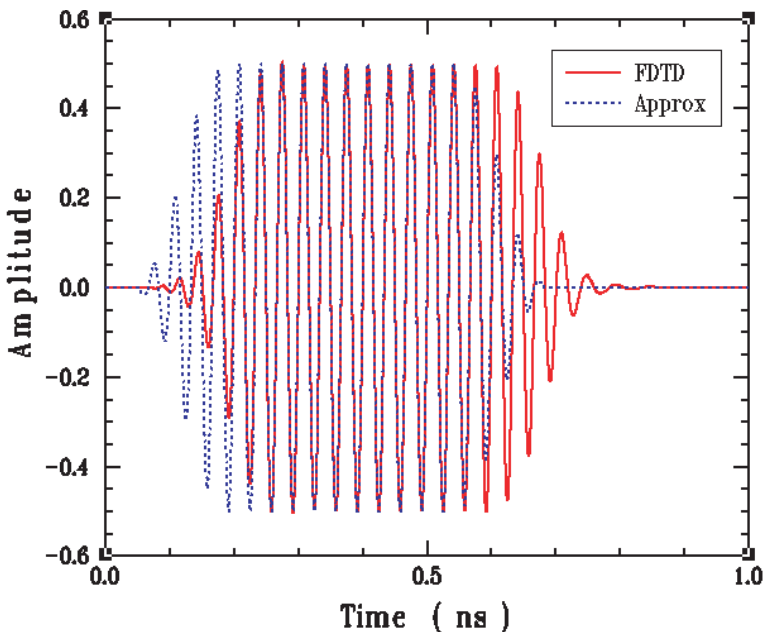


**Figure 1.5** A comparison of the FDTD-generated time history of a wave propagating in a dispersive Drude medium and an approximate solution consisting of a causal propagating envelope and the expected NIR sinusoidal signal shows very good agreement in the steady-state region away from the leading and trailing edges where dispersion plays a significant role. From [44]. Copyright © 2003 by the American Physical Society.

The analogous problem in a nondispersive DNG medium was also considered, and it was shown that the solution to this problem is not causal, in agreement with similar observations given in [18]. An approximate solution was constructed that combined a causal envelope with a sinusoid which has the nondispersive NIR properties; it compared favorably with the FDTD results for the dispersive DNG case, as shown in Figure 1.5. It was thus demonstrated that causal results do indeed require the presence of dispersion in DNG media and that the dispersion is responsible for a dynamic reshaping of the pulse to maintain causality. The CW portions of a modulated pulse (i.e., excluding its leading and trailing edges) do obey all of the NIR effects expected from a time-harmonic analysis in a bandlimited “nondispersive” DNG medium. Therefore, one can conclude that the CW analyses of DNG media are credible as long as very narrow bandwidth pulse trains are considered for any practical realizations. This has been the case in all of the experimental results reported to date of which we are aware. Moreover, time delays for the realization of the NIR effects are inherent in the processes dictated by the dispersive nature of the physics governing these media.

## 1.5 SCATTERING FROM A DNG SLAB

The reflection and transmission coefficients associated with a normally incident plane wave that scatters from a DNG slab embedded in a medium have been derived. The geometry is shown in Figure 1.6. The slab has an infinite extent in the transverse directions; it has a thickness  $d$  in the direction of propagation of the incident plane wave. Let the medium before and after the slab be characterized by  $\varepsilon_1, \mu_1$  and the slab be characterized by  $\varepsilon_2, \mu_2$ . For a normally incident plane wave, the reflection and transmission coefficients for the slab are

$$R = \frac{\eta_2 - \eta_1}{\eta_2 + \eta_1} \frac{1 - e^{-j2k_2 d}}{1 - [(\eta_2 - \eta_1)/(\eta_2 + \eta_1)]^2 e^{-j2k_2 d}} \quad (1.12)$$

$$T = \frac{4\eta_2\eta_1}{(\eta_2 + \eta_1)^2} \frac{e^{-jk_2 d}}{1 - [(\eta_2 - \eta_1)/(\eta_2 + \eta_1)]^2 e^{-j2k_2 d}}$$

where the wavenumber  $k_i = \omega\sqrt{\varepsilon_i}\sqrt{\mu_i}$  and wave impedance  $\eta_i = \sqrt{\mu_i}/\sqrt{\varepsilon_i}$  for  $i = 1, 2$ . For the case of normal incidence, if we consider a matched DNG medium, one would have  $\eta_2 = \eta_1$  so that  $R = 0$  and  $T = e^{-jk_2 d} = e^{+j|k_2|d}$ . The

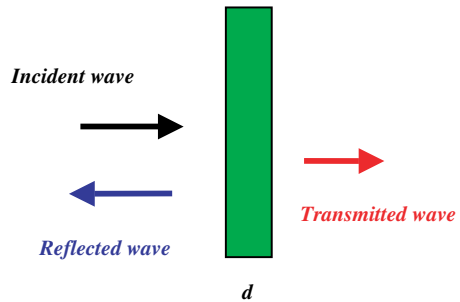


**Figure 1.6** Plane-wave scattering from slab of thickness  $d$ .

medium would thus add a positive phase to the wave traversing the slab, whereas in a DPS medium the wave would experience a negative phase variation. This means that a matched DNG slab could be used to compensate for phase changes incurred by passage of a plane wave through a DPS slab; that is, one can force  $k_{\text{DPS}}d_{\text{DPS}} + k_{\text{DNG}}d_{\text{DNG}} = 0$ . This phase compensation, to be discussed later in this chapter, is an interesting feature of DNG metamaterials that can lead to exciting potential applications.

When the plane wave is obliquely incident, Eq. (1.12) is straightforwardly modified by introducing the transverse impedance and longitudinal wavenumber components. If, in addition, the incident wave is evanescent, that is, when the transverse component of the wave vector of the incident wave is greater than the wavenumber of the medium ( $k_t^2 > \omega^2\mu_1\varepsilon_1$  and  $k_t^2 > \omega^2\mu_2\varepsilon_2$ ), the transverse wave impedance in each medium (with a no-loss assumption) becomes purely imaginary, that is,  $\eta_{1,\text{transverse}} = jX_{1,\text{transverse}}$  and  $\eta_{2,\text{transverse}} = jX_{2,\text{transverse}}$ , and the longitudinal component of the wave vector in each medium also becomes purely imaginary, that is,  $k_{1,\text{longitudinal}} = j\alpha_1$  and  $k_{2,\text{longitudinal}} = j\alpha_2$  [45,46]. (The proper choice of sign for  $\alpha_1$  and  $\alpha_2$  will be discussed shortly.) However, it can be shown that this transverse wave impedance in the DPS and DNG media have opposite signs; that is, if one has a capacitive reactance, the other will have an inductive reactance so that  $\text{sgn}[X_{1,\text{transverse}}] = -\text{sgn}[X_{2,\text{transverse}}]$ , where  $\text{sgn}(x) = +1 (-1)$  for  $x > 0 (x < 0)$  [45, 46]. When we choose the so-called matched condition for which  $\mu_2 = -\mu_1$  and  $\varepsilon_2 = -\varepsilon_1$ , one can demonstrate that  $X_{1,\text{transverse}} = -X_{2,\text{transverse}}$ . Inserting these features into the generalized form of Eq. (1.12), one would observe that again  $R = 0$ , but now  $T = e^{-jk_{2,\text{longitudinal}}d} = e^{\alpha_2d}$ . What is the proper sign for  $\alpha_2$ ? A detailed discussion, including a variety of physical insights, on this issue can be found in, for example, [45,46]. Here we briefly review this point. It is known that at the interface between a DPS and a DNG medium, the tangential components of the electric and magnetic fields should be continuous according to Maxwell equations. However, since the permittivity and the permeability of these two media each has opposite signs, the normal spatial derivatives (normal with respect to the interface) of these tangential components are discontinuous at this boundary [19]. In other words, if the tangential component of the electric field (or the magnetic field) is decreasing as the observation point gets closer to this interface from the DPS side, the same tangential component should be increasing as the observer is receding from the interface in the DNG side. Moreover, one should remember that according to Eq. (1.12) the overall reflection coefficient for the “incident” evanescent wave in this case is  $R = 0$ . Therefore, as this evanescent wave reaches the first interface of the matched DNG slab from the DPS region, it is decaying, that is,  $\alpha_1 < 0$ , and no “reflected” evanescent wave will be present in this DPS medium. However, as we move just past the first interface into the DNG region, the tangential components of the field in the vicinity of the interface inside the DNG region should “grow” in order to satisfy the discontinuity condition of the normal spatial derivative mentioned above. (Note that if the evanescent wave decayed inside this matched DNG slab, the tangential components of the field at the DPS–DNG interface would have similar slopes, inconsistent with the boundary condition

mentioned above.) Therefore, in the transmission coefficient expression  $T = e^{\alpha_2 d}$ , one should have  $\alpha_2 > 0$ . As a result, such a matched DNG slab can compensate the decay of the evanescent wave in the DPS region through the growth of the evanescent wave inside the DNG slab. This issue was originally pointed out by Pendry in [7] and is the basis behind the idea of subwavelength focusing and “perfect” lensing [7]. We emphasize that this growth of an evanescent wave inside the DNG slab does not violate any physical law, since each of these *evanescent* waves carries no real power, and indeed this scenario represents the presence of an interface resonance at the boundary between the DPS and DNG regions [45,46]. Furthermore, this phenomenon can also be described and justified using distributed circuit elements, which provide further insight into related features associated with this problem [45,46].

An interesting question arises here: If one gets a growing evanescent wave inside the slab, as justified above for the case of a finite-thickness matched DNG slab, what should one see for a semi-infinite matched DNG medium when an “incident” evanescent wave is approaching this interface? In other words, when we have a single interface between matched semi-infinite DPS and semi-infinite DNG media, what will happen for an ‘incident’ evanescent wave? This is a markedly different problem. In this case, we only deal with one interface, and the reflection and transmission coefficients for such an interface can be easily expressed as

$$R_{\text{DPS-DNG}} = \frac{\eta_{2,\text{transverse}} - \eta_{1,\text{transverse}}}{\eta_{2,\text{transverse}} + \eta_{1,\text{transverse}}}$$

and

$$T_{\text{DPS-DNG}} = \frac{2\eta_{2,\text{transverse}}}{\eta_{2,\text{transverse}} + \eta_{1,\text{transverse}}}$$

For the matched condition, as discussed above, we have  $\eta_{1,\text{transverse}} = jX_{1,\text{transverse}}$  and  $\eta_{2,\text{transverse}} = jX_{2,\text{transverse}}$  with  $X_{1,\text{transverse}} = -X_{2,\text{transverse}}$ . Therefore, one gets  $R_{\text{DPS-DNG}} = \infty$  and  $T_{\text{DPS-DNG}} = \infty$ , which implies that there is an interface resonance at this boundary. This is indeed another indication that such an interface can indeed support a surface plasmon wave, which is an important factor in understanding the behavior of this interface [45,46]. Similarly, the Fresnel “reflection” and “transmission” coefficients for an incident evanescent wave for this configuration become infinite (the circuit analog of this phenomenon has also been studied [45,46]). This is analogous to exciting a resonant structure (such as an  $L$ - $C$  circuit) at its resonant frequency, which also leads to infinite fields in the structure when there are no losses present. Consequently, when there is a source in front of the interface between two semi-infinite matched DNG and DPS media, a resonant surface wave may be excited along the interface, resulting in an infinitely large field value. However, the fields on both sides of this interface, albeit infinitely large, *decay* exponentially as they move away from it; that is, the field distribution represents a surface wave propagating along the interface. This explains and justifies the presence of  $R_{\text{DPS-DNG}} = \infty$  and  $T_{\text{DPS-DNG}} = \infty$ . In summary, for a single matched DPS-DNG interface, one finds an evanescent wave in each medium whose amplitude is infinite at the interface but decays

exponentially as the wave recedes away from it. On the other hand, for a matched DNG slab the presence of two interfaces allows a resonant interaction that produces a net exponential growth of the evanescent wave components inside the slab despite their exponential decay outside of it.

## 1.6 BACKWARD WAVES

Consider the source problems shown in Figure 1.7. A current sheet of the form

$$\mathbf{J}_s = I_0 e^{-jk_{0x}x} \delta(z) \hat{x} \quad (1.13)$$

is located on the interface between two semi-infinite media. In one case both regions are DPS media, and in the other one is a DPS medium and the other is a DNG medium. The wavenumbers in each medium satisfy the dispersion relation

$$k_{i,x}^2 + k_{i,z}^2 = k_i^2 = \omega^2 \varepsilon_i \mu_i \quad (1.14)$$

where region 1 labels  $z > 0$  and region 2 labels  $z < 0$ . Boundary conditions require the wave numbers tangential to the interface be the same in each medium, that is,  $k_{1,x} = k_{2,x} = k_{0x}$ ; thus for propagating waves they also require the propagation constants normal to the interface be given as

$$k_z^{\text{DPS}} = +\sqrt{\omega^2 \varepsilon_{\text{DPS}} \mu_{\text{DPS}} - k_{0x}^2} \quad k_z^{\text{DNG}} = -\sqrt{\omega^2 \varepsilon_{\text{DNG}} \mu_{\text{DNG}} - k_{0x}^2} \quad (1.15)$$

The wave vectors in each region are thus given by the expressions

$$\mathbf{k}_1 = k_{0x} \hat{x} + k_{1z} \hat{z} \quad \mathbf{k}_{2,\text{DPS}} = k_{0x} \hat{x} - k_{2z} \hat{z} \quad \mathbf{k}_{2,\text{DNG}} = k_{0x} \hat{x} + |k_{2z}| \hat{z} \quad (1.16)$$

Similarly, the Poynting's vector in each region is determined to be

$$\langle \mathbf{S}_1 \rangle(x, y, z, \omega) = \frac{1}{2\omega \varepsilon_1} \left| \frac{k_{2z}}{\varepsilon_2} \frac{I_0}{k_{1z}/\varepsilon_1 + k_{2z}/\varepsilon_2} \right|^2 (k_{0x} \hat{x} + k_{1z} \hat{z}) \quad (1.17)$$

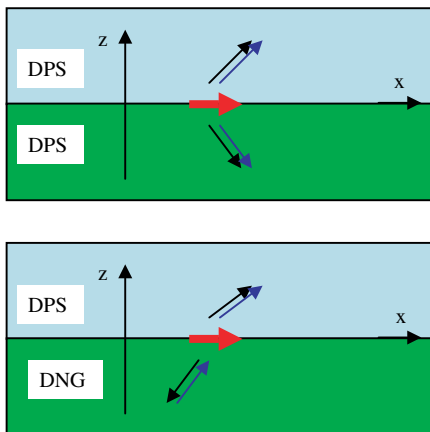


**Figure 1.7** Current sheet located at interface between two semi-infinite half spaces. Blue arrows represent the wave vectors, black arrows the Poynting vectors.

$$\begin{aligned}\langle \mathbf{S}_{2,\text{DPS}} \rangle(x, y, z, \omega) &= \frac{1}{2\omega\varepsilon_2} \left| \frac{k_{1z}}{\varepsilon_1} \frac{I_0}{k_{1z}/\varepsilon_1 + k_{2z}/\varepsilon_2} \right|^2 (k_{0x}\hat{x} - k_{2z}\hat{z}) \\ \langle \mathbf{S}_{2,\text{DNG}} \rangle(x, y, z, \omega) &= \frac{1}{2\omega|\varepsilon_2|} \left| \frac{k_{1z}}{\varepsilon_1} \frac{I_0}{k_{1z}/\varepsilon_1 + |k_{2z}|/|\varepsilon_2|} \right|^2 (-k_{0x}\hat{x} - |k_{2z}|\hat{z})\end{aligned}\quad (1.18)$$

Thus one finds that the Poynting vector and wave vector directions are the same when both regions are DPS media and the generated waves are in the forward direction, that is, in the direction of positive phase advance along the source. In contrast, the Poynting vector in the DNG medium is pointed causally away from the source and is opposite to the wave vector direction, which is toward the source. Moreover, the flow of power of the wave generated in the DNG medium is opposite to the positive phase direction of the source. The backward-wave nature of the wave generated in the DNG medium is thus established. The details of this problem can be found in [47].

## 1.7 NEGATIVE REFRACTION

The phenomenon of negative refraction is studied by considering the scattering of a wave that is obliquely incident on a DPS–DNG interface as shown in Figure 1.8. Enforcing the electromagnetic boundary conditions at the interface, one obtains the law of reflection and Snell’s Law from phase matching:

$$\theta_{\text{refl}} = \theta_{\text{inc}} \quad \theta_{\text{trans}} = \text{sgn}(n_2) \sin^{-1} \left( \frac{n_1}{|n_2|} \sin \theta_{\text{inc}} \right) \quad (1.19)$$

Note that if the index of refraction of a medium is negative, then the refracted angle, according to Snell’s law, should also become “negative.” This suggests that the refraction is anomalous, and the refracted angle is on the same side of the interface normal as the incident angle is. The wave and Poynting vectors associated with this oblique scattering problem are also obtained:

$$\begin{aligned}\mathbf{k}_{\text{inc}} &= k_1 (\cos \theta_{\text{inc}} \hat{z} + \sin \theta_{\text{inc}} \hat{x}) \\ \mathbf{k}_{\text{refl}} &= k_1 (-\cos \theta_{\text{inc}} \hat{z} + \sin \theta_{\text{inc}} \hat{x}) \\ \mathbf{k}_{\text{trans}} &= k_2 (\cos \theta_{\text{trans}} \hat{z} + \sin \theta_{\text{trans}} \hat{x})\end{aligned}\quad (1.20)$$

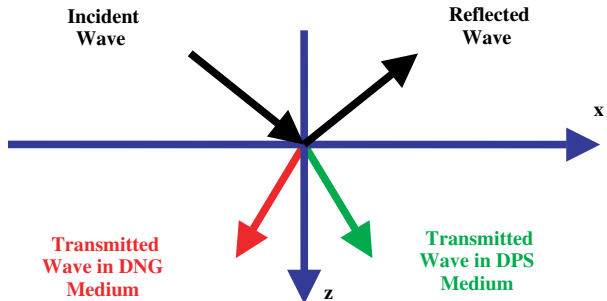


**Figure 1.8** Geometry of the scattering of a wave obliquely incident upon a DPS–DNG interface.

$$\begin{aligned}
\mathbf{S}_{\text{inc}} &= \frac{1}{2} \frac{|E_0|^2}{\eta_1} (\cos \theta_{\text{inc}} \hat{z} + \sin \theta_{\text{inc}} \hat{x}) \\
\mathbf{S}_{\text{refl}} &= \frac{1}{2} \frac{|RE_0|^2}{\eta_1} (-\cos \theta_{\text{inc}} \hat{z} + \sin \theta_{\text{inc}} \hat{x}) \\
\mathbf{S}_{\text{trans}} &= \frac{1}{2} \frac{|TE_0|^2}{\eta_2} (\cos \theta_{\text{trans}} \hat{z} + \sin \theta_{\text{trans}} \hat{x})
\end{aligned} \tag{1.21}$$

Assuming that the transmitted wave is propagating in a DPS medium, it is clear that the Poynting and wave vectors are in the same direction. However, if the transmitted wave is propagating in a DNG medium, the index is less than zero and one obtains immediately from Snell's law that

$$\begin{aligned}
\mathbf{k}_{\text{trans}} &= -|n_2| \frac{\omega}{c} (\cos |\theta_{\text{trans}}| \hat{z} - \sin |\theta_{\text{trans}}| \hat{x}) \\
\mathbf{S}_{\text{trans}} &= \frac{1}{2} \frac{|TE_0|^2}{\eta_2} (\cos |\theta_{\text{trans}}| \hat{z} - \sin |\theta_{\text{trans}}| \hat{x})
\end{aligned}$$

so that the wave and Poynting vectors point in opposite directions, the Poynting vector being directed in a causal direction away from the interface.

This negative-refraction behavior was verified with FDTD calculations [22]. The electric field intensity distributions were obtained with the 2D FDTD simulator when a  $f_0 = 30$  GHz (needless to say, this choice is arbitrary; the numerical results presented here can be obtained at any frequency with a proper scaling of

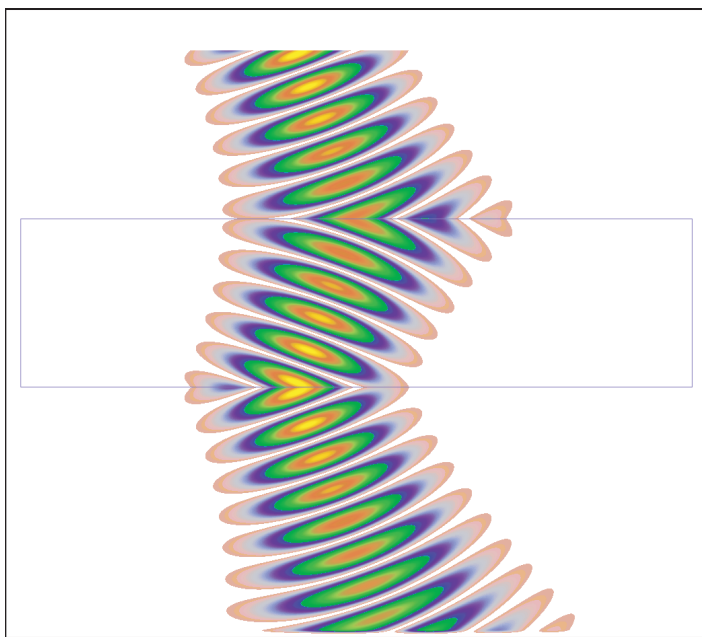


**Figure 1.9** The NIR behavior has been confirmed with FDTD simulations. From [22]. Copyright © 2003 by The Optical Society of America.

the parameters) perpendicularly polarized CW Gaussian beam is incident on a DPS–DNG interface with  $\theta_{\text{inc}} = 20^\circ$ . To reduce the effect of reflection and thus to observe the negative refraction more clearly, the parameters of these slabs were chosen such that the slabs are impedance matched to free space. Therefore, the electric and magnetic Drude models were selected to be identical, that is,  $\omega_{pe} = \omega_{pm} = \omega_p$  and  $\Gamma_e = \Gamma_m = \Gamma$ . Only low loss values were considered by setting  $\Gamma = 10^{+8} s^{-1} \ll \omega_p$ . This means that the index of refraction had the form

$$\begin{aligned} n(\omega) &= \sqrt{\frac{\varepsilon(\omega)}{\varepsilon_0}} \sqrt{\frac{\mu(\omega)}{\mu_0}} = 1 - \frac{\omega_p^2}{\omega(\omega - j\Gamma)} = 1 - \frac{\omega_p^2}{\omega^2 + \Gamma^2} - j \frac{\Gamma}{\omega} \frac{\omega_p^2}{\omega^2 + \Gamma^2} \\ &\approx 1 - \frac{\omega_p^2}{\omega^2} - j \frac{\Gamma \omega_p^2}{\omega^3} \end{aligned} \quad (1.22)$$

The DNG slab had  $n_{\text{real}}(\omega_0) \approx -1$ , by setting  $\omega_p = 2\pi\sqrt{2}f_0 = 2.66573 \times 10^{11}$  rad/s and, hence,  $\Gamma = 3.75 \times 10^{-4}\omega_p$ . As can be seen in Figure 1.9, the negative angle of refraction is clearly seen. The refracted angle is equal and opposite to the angle of incidence. The discontinuities in the derivatives of the fields at the DPS–DNG interfaces (i.e., the so-called V-shaped patterns at both interfaces) are clearly seen. A simulation movie of this case is available in [22].

## 1.8 PHASE COMPENSATION WITH A DNG MEDIUM

As we reviewed in our recent paper [48], one of the interesting features of DNG media is their ability to provide phase compensation or phase conjugation due to their negative refraction. Here, we provide an illustrative example to highlight the insight behind this phenomenon. Consider a slab of conventional lossless DPS material with positive index of refraction  $n_1$  and thickness  $d_1$  and a slab of lossless DNG metamaterial with negative refractive index  $-|n_2|$  and thickness  $d_2$ . Although not necessary, but for the sake of simplicity in the argument, we assume that each of these slabs is impedance matched to the outside region (e.g., free space). Let us take a monochromatic uniform plane wave normally incident on this pair of slabs. As this wave propagates through the slab, the phase difference between the exit and entrance faces of the first slab is obviously  $n_1 k_0 d_1$ , where  $k_0 \equiv \omega \sqrt{\varepsilon_0 \mu_0}$ , while the total phase difference between the front and back faces of this two-layer structure is  $|n_1| k_0 d_1 - |n_2| k_0 d_2$ , implying that whatever phase difference is developed by traversing the first slab, it can be decreased and even compensated for by traversing the second slab. If the ratio of  $d_1$  and  $d_2$  is chosen to be  $d_1/d_2 = |n_2|/|n_1|$  at the given frequency, then the total phase difference between the front and back faces of this two-layer structure will become zero. This means that the DNG slab acts as a phase compensator in this structure [19,27]. We should note that such phase compensation/conjugation does not depend on the *sum* of thicknesses,  $d_1 + d_2$ , rather it depends on the *ratio* of  $d_1$  and  $d_2$ . So, in principle,  $d_1 + d_2$  can be any value as long as  $d_1/d_2$  satisfies the above condition. Therefore, even though this two-layer structure is present, the wave traversing this structure would not experience any phase difference

between the input and output faces. This feature can lead to several interesting ideas in device and component designs, as will be discussed later.

Such phase compensation has been verified using the FDTD simulator, as shown in Figure 1.10. The FDTD predicted electric field intensity distribution for a perpendicularly polarized CW Gaussian beam incident on this DPS–DNG slab pair is shown. A Gaussian beam was launched toward the DPS–DNG slab pair, each slab having a thickness of  $2\lambda_0$ . The DPS slab had  $n(\omega) = +3$ , while the DNG slab had  $n_{\text{real}}(\omega_0) \approx -3$ . As is evident from Figure 1.10, the beam expands

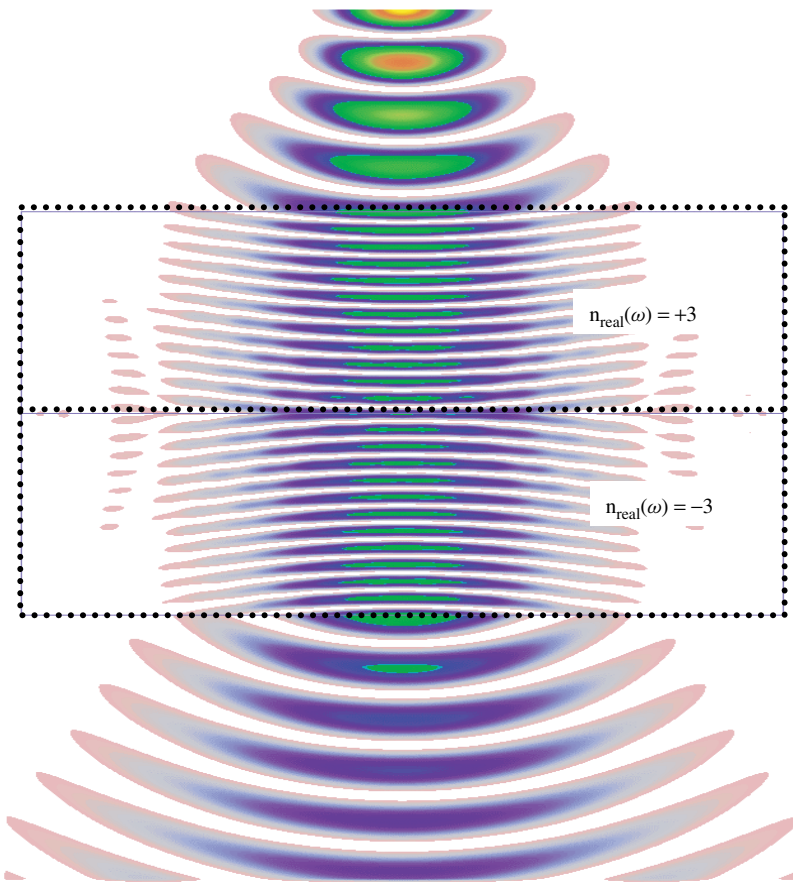


**Figure 1.10** FDTD predicted electric field intensity distribution for phase compensator–beam translator system DPS–DNG stacked pair. The Gaussian beam is normally incident on a stack of two slabs, the first being a DPS slab with  $n_{\text{real}}(\omega) = +3$  and the second being a DNG slab with  $n_{\text{real}}(\omega_0) \approx -3$ . The initial beam expansion in the DPS slab is compensated by its refocusing in the DNG slab. The Gaussian beam is translated from the front face of the system to its back face with only  $-0.323$  dB attenuation over the  $4\lambda_0$  distance.

in the DPS slab and then the negative-refraction property refocuses it in the DNG slab, and the waist of the intensity of the input beam is recovered at the back face. The electric field intensity could, in principle, be maintained over the total thickness of  $4\lambda_0$ . There is only a  $-0.323$ -dB (7.17%) reduction in the peak value of the intensity of the beam when it reaches the back face. Moreover, the phase of the beam at the output face of the stack is the same as its value at the entrance face. Therefore, the beam emerges at the output of the slab pair in phase with the input beam and only slightly smaller in amplitude. Thus the DPS–DNG slab pair, in essence, translates the field from one location to another with low losses; that is, it acts as a beam translator.

Using multiple matched DPS–DNG stacks, one could produce a phase-compensated, time-delayed, waveguiding system. Each pair in the stack would act as shown in Figure 1.10. Thus the phase compensation–beam translation effects would occur throughout the entire system. Moreover, by changing the index of any of the DPS–DNG pairs, one changes the speed at which the beam traverses that slab pair. Consequently, one can change the time for the beam to propagate from the entrance face to the exit face of the entire DPS–DNG stack. In this manner one could realize a volumetric, low-loss time delay line for a Gaussian beam system.

This phase compensation can lead to a wide variety of potential applications that could have a large impact on a number of engineering systems. One such set of applications offers the possibility of having subwavelength, electrically small cavity resonators and waveguides with lateral dimension below diffraction limits. These ideas are briefly reviewed in Chapter 2.

## 1.9 DISPERSION COMPENSATION IN A TRANSMISSION LINE USING A DNG MEDIUM

---

The DNG medium, because of its dispersive nature, might also be used as an effective dispersion compensation device for time-domain applications. The dispersion produces a variance of the group speed of the signal components as they propagate in the DNG medium. Cheng and Ziolkowski have considered the use of volumetric DNG metamaterials for the modification of the propagation of signals along a microstrip transmission line [49]. If one could compensate for the dispersion along such transmission lines, signals propagating along them would not become distorted. This could lead to a simplification of the components in many systems. Microstrip dispersion can be eliminated by correcting for the frequency dependence of the effective permittivity associated with this type of transmission line. As shown in [50, 51], for a microstrip transmission line of width  $w$  and a conventional dielectric substrate height  $h$  one has the approximate result for the effective relative permittivity of the air–substrate–microstrip system:

$$\varepsilon_{\text{eff}}(f) = \varepsilon_r - \frac{\varepsilon_r - \varepsilon_{es}}{1 + G(f/f_d)^2} \quad (1.23)$$

where the constants

$$f_d = \frac{Z_c}{2\mu_0 h} \quad G = 0.6 + 0.0009Z_c$$

the characteristic impedance is

$$Z_c \cong \frac{1}{2\pi} \sqrt{\frac{\mu_0}{\varepsilon_{es}\varepsilon_0}} \log \left[ F_1 \frac{h}{w} + \sqrt{1 + \left(2\frac{h}{w}\right)^2} \right]$$

with  $F_1 = 6 + (2\pi - 6) \exp[-(30.666h/w)^{0.7528}]$ , and the electrostatic relative permittivity is

$$\varepsilon_{es} \cong \frac{\varepsilon_r + 1}{2} + \left(\frac{\varepsilon_r - 1}{2}\right) \left[1 + 10\left(\frac{h}{w}\right)\right]^{-ab}$$

with

$$a = 1 + \frac{1}{49} \log \left[ \frac{(w/h)^4 + (w/52h)^2}{(w/h)^4 + 0.432} \right] + \frac{1}{18.7} \log \left[ 1 + \left(\frac{1}{18.1} \frac{w}{h}\right)^3 \right]$$

$$b = 0.564 \left(\frac{\varepsilon_r - 0.9}{\varepsilon_r + 3.0}\right)^{0.053}$$

The goal is to design a length of metamaterial-loaded transmission line that can be included in some manner with the same length of microstripline to make the paired system dispersionless; that is, we want to produce a dispersion-compensated segment of transmission line. This means we want to introduce a metamaterial with relative permittivity  $\varepsilon_{\text{MTM}}$  and permeability  $\mu_{\text{MTM}}$  so that the overall relative permittivity and permeability of the system is

$$\frac{\varepsilon(f)}{\varepsilon_0} = \varepsilon_{\text{eff}}(f) + \varepsilon_{\text{MTM}}(f) \quad \frac{\mu(f)}{\mu_0} = 1 + \mu_{\text{MTM}}(f) \quad (1.24)$$

in such a manner that the wave impedance in the metamaterial remains the same as it is in the original substrate, that is,

$$Z = \sqrt{\frac{\mu(f)}{\varepsilon(f)}} = Z_0 \sqrt{\frac{1 + \mu_{\text{MTM}}(f)}{\varepsilon_{\text{MTM}}(f) + \varepsilon_{\text{eff}}(f)}} = Z_0 \sqrt{\frac{1}{\varepsilon_{\text{eff}}(f)}} \quad (1.25)$$

and the index of refraction in the medium compensates for the dispersion effects associated with the microstrip geometry itself; that is, the effective index of the pair becomes that of free space,

$$n_{\text{eff}}(f) = \sqrt{\varepsilon_{\text{eff}}(f)} + \sqrt{\frac{\varepsilon(f)}{\varepsilon_0} \frac{\mu(f)}{\mu_0}}$$

$$= \sqrt{\varepsilon_{\text{eff}}(f)} + \sqrt{\varepsilon_{\text{eff}}(f) + \varepsilon_{\text{MTM}}(f)} \sqrt{1 + \mu_{\text{MTM}}(f)} = 1 \quad (1.26)$$

These conditions are satisfied if  $\varepsilon_{\text{eff}}(f)[1 + \mu_{\text{MTM}}(f)] = \varepsilon_{\text{MTM}}(f) + \varepsilon_{\text{eff}}(f)$  so that

$$\mu_{\text{MTM}}(f) = \frac{1}{\sqrt{\varepsilon_{\text{eff}}(f)}} - 1 \quad \varepsilon_{\text{MTM}}(f) = \varepsilon_{\text{eff}}(f)\mu_{\text{MTM}}(f) \quad (1.27)$$

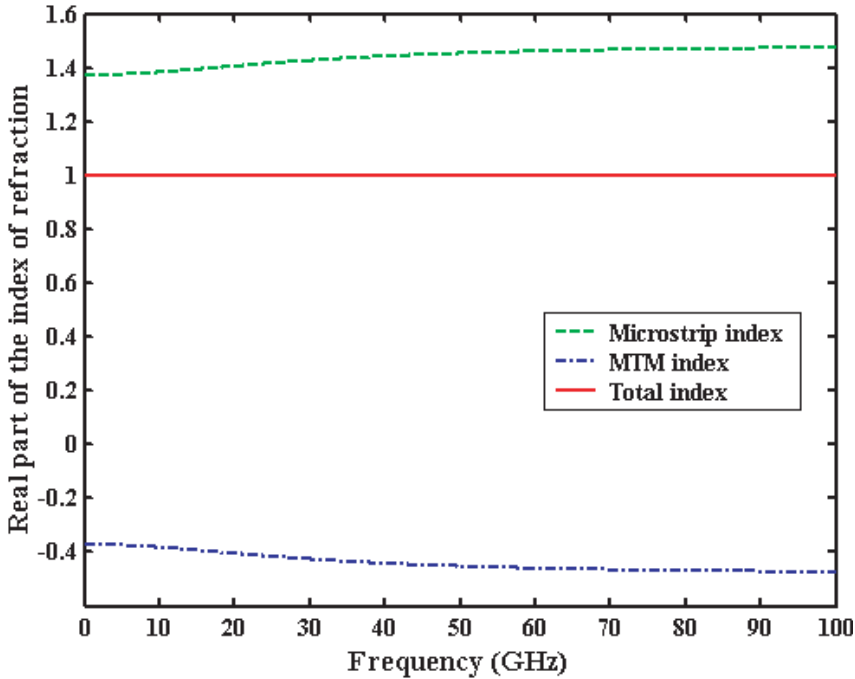


**Figure 1.11** Real part of index of refraction of microstrip only, of metamaterial (MTM) only, and total MTM-dispersion-compensated transmission line.

We note that the effective permittivity and permeability of such a metamaterial should be negative, implying that a DNG material must be utilized for this purpose. [The range of validity of condition (1.27) should be consistent with that of the effective medium approximation (1.23).] A plot of the index of refraction of the uncompensated line, the metamaterial compensator, and the dispersion-compensated line is shown in Figure 1.11 for a microstrip transmission line at 10 GHz using Roger’s Duroid 5880 substrate. The substrate had the relative permittivity  $\epsilon_r = 2.2$  and its height was  $h = 31$  mils  $= 0.7874$  mm. The width of the transmission line was  $w = 2.428$  mm  $= 95.6$  mils to achieve a  $50 \Omega$  impedance. As shown in Figure 1.11, in principle, complete dispersion compensation is theoretically possible.

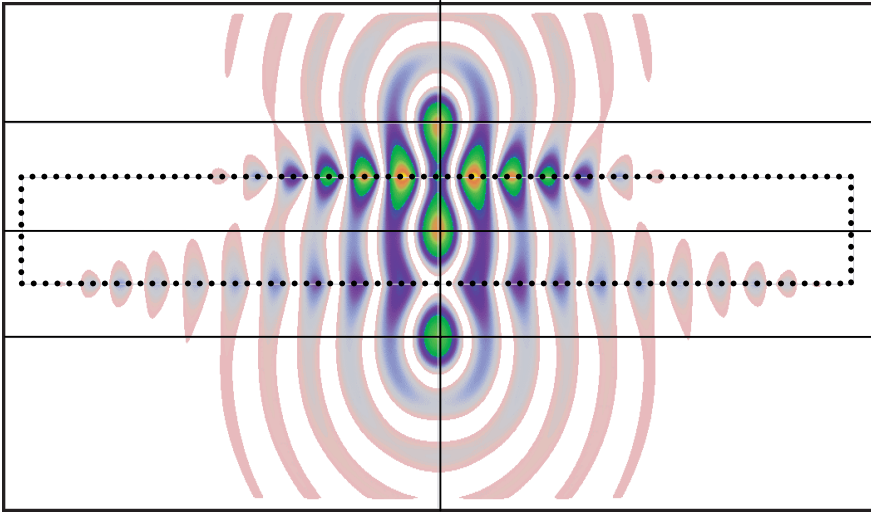
## 1.10 SUBWAVELENGTH FOCUSING WITH A DNG MEDIUM

Another interesting potential application of a DNG medium that results from its negative-refraction properties was first theoretically suggested by Pendry [7]. It is the idea of a “perfect lens” or focusing beyond the diffraction limit. In his analysis of the image formation process in a flat slab of lossless DNG material, Pendry

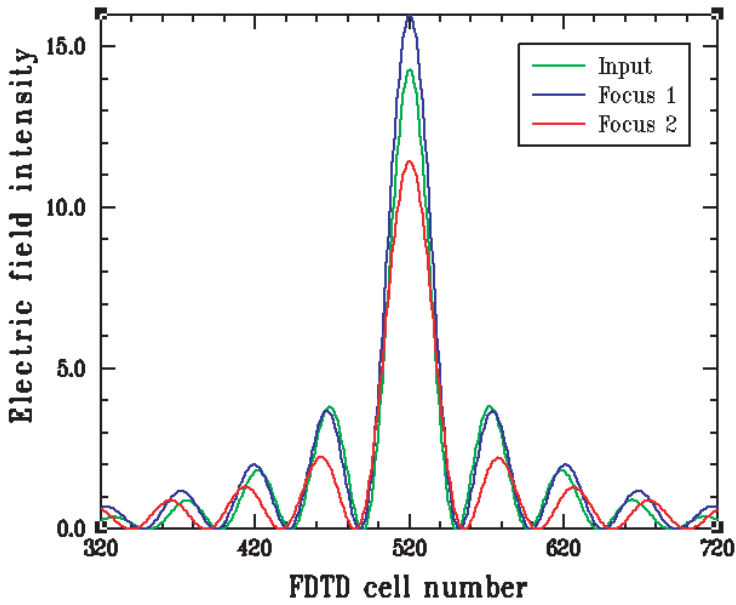
showed that the evanescent spatial Fourier components can be ideally reconstructed in addition to the faithful reconstruction of all the propagating spatial Fourier components. The evanescent wave reconstruction is due to the presence of the “growing exponential effect” in the DNG slab discussed in Section 1.5. This effect in theory leads to the formation of an image with a resolution higher than the conventional limit. His idea has motivated much interest in studying wave interactions with DNG media.

Various theoretical and experimental works by several groups have explored this possibility; they have shown the possibility and limitations of subwavelength focusing using a slab of DNG or negative-index metamaterials [52, 53]. The subwavelength focusing in the planar 2D structures made of negative-index transmission lines has also been investigated [31]. The presence of the growing exponential in the DNG slab has also been explained and justified using the equivalent distributed circuit elements in transmission line model [46]. It has also been shown that “growing evanescent envelopes” for the field distributions can be achieved in a suitably designed, periodically layered stacks of frequency-selective surfaces (FSSs) [54].

It was shown analytically in [12] that the perfect-focus solution exists only for the frequency-independent, lossless DNG slab case for which  $\epsilon_r = \mu_r = -1$ . For all other cases, a line source will produce paraxial foci. If the line source is located  $z_0$  away from the front face of the slab, the foci produced by a DNG slab have been shown analytically [12] to occur at the distances  $z_{f1} = |n_2||z_0|$  and  $z_{f1} = d(1 + 1/|n_2|) - |z_0|$  away from that face and the source. Thus for an  $n_{\text{real}}(\omega_0) \approx -1$  planar slab of thickness  $d$ , the first focus is located at  $z_{f1} = |z_0|$  and the second is at  $z_{f2} = 2d - |z_0|$ . The electric field intensity predicted by the FDTD simulator for a lossy Drude slab with  $n_{\text{real}}(\omega_0) \cong -1$  and  $\Gamma = 10^{-5}\omega_0$  is shown in Figure 1.12a. The line source is 50 cells in front of a 100-cell-deep slab. The location of the source and the expected locations of the two foci are indicated by the intersections of the vertical and horizontal black lines. The transverse profiles of the intensity along the horizontal lines are shown in Figure 1.12b. While the foci appear where expected, they are not perfect. As explained in [12], the perfect focus is not obtained because of the presence of dispersion and the large generation of surface waves which take energy away from the focusing mechanism. The transverse full width at half maximum (FWHM) of the input intensity and the intensities at  $z_{f1} = 50$  cells and  $z_{f2} = 150$  cells from the front interface are 29, 31, and 34 cells, respectively. Nonetheless, since a cell is  $\lambda_0/100$ , these distances are all subwavelength. The appearance of the paraxial foci is demonstrated in Figure 1.13a. The line source is 10 cells in front of a 120-cell-deep lossy Drude slab with  $n_{\text{real}}(\omega_0) \cong -6$  and  $\Gamma = 10^{-5}\omega_0$ . The location of the source and the expected locations of the two foci are again indicated by the intersections of the vertical and horizontal black lines. The paraxial focusing (channeling) of the beam within the slab is readily apparent. The waist of the beam occurs where the focus within the slab is located. The transverse profiles of the intensity along the front interface and along the horizontal foci lines are shown in Figure 1.13b. The FWHM of these profiles are, respectively, 23, 28,

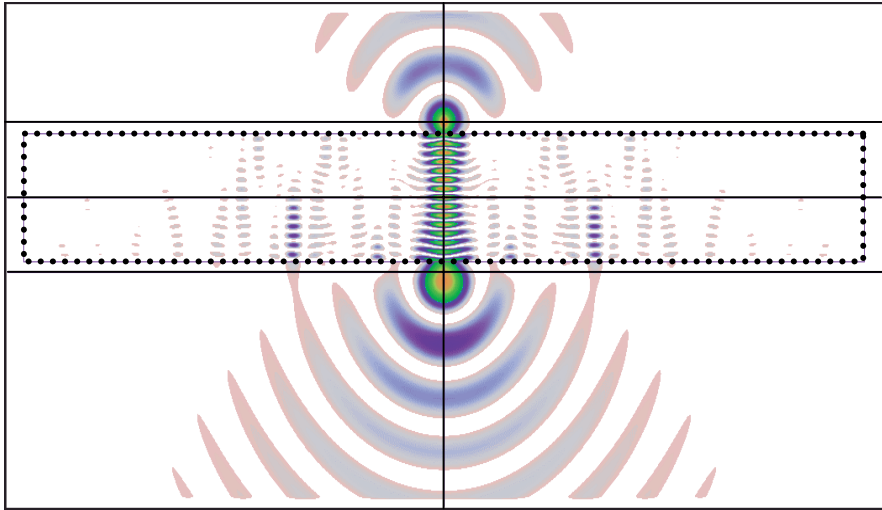


(a)

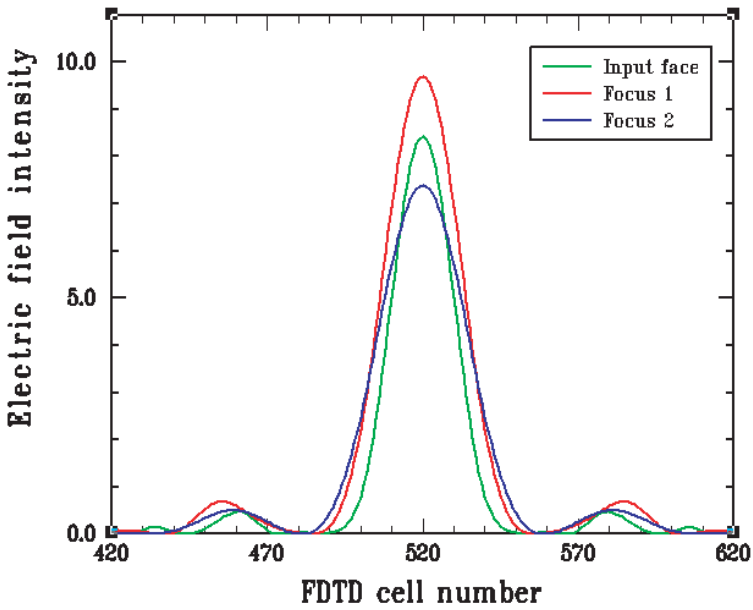


(b)

**Figure 1.12** (a) The FDTD predicted electric field intensity distribution illustrates the focusing of the field generated by a line source in a  $n_{\text{real}}(\omega_0) \approx -1$  DNG slab. (b) Transverse profiles of the electric field intensity distribution at various locations.



(a)



(b)

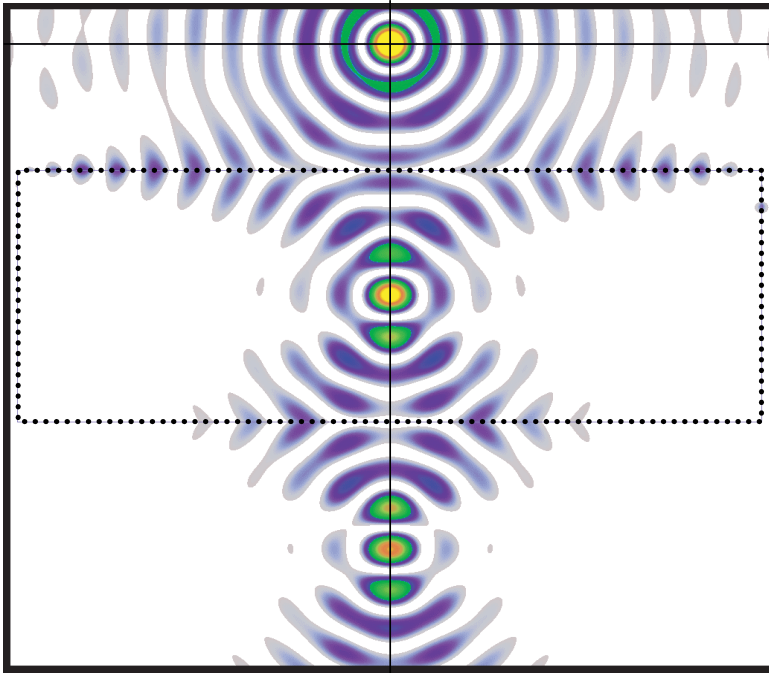
**Figure 1.13** (a) The FDTD predicted electric field intensity distribution illustrates the focusing of the field generated by a line source in a  $n_{\text{real}}(\omega_0) \approx -6$  DNG slab. (b) Transverse profiles of electric field intensity distribution at various locations. Channeling of the beam in the DNG slab is observed; the wings of the beam are seen to feed the center of the beam.

and 32 cells. Again, the FWHM of the intensity profile of the beam at the foci is subwavelength.

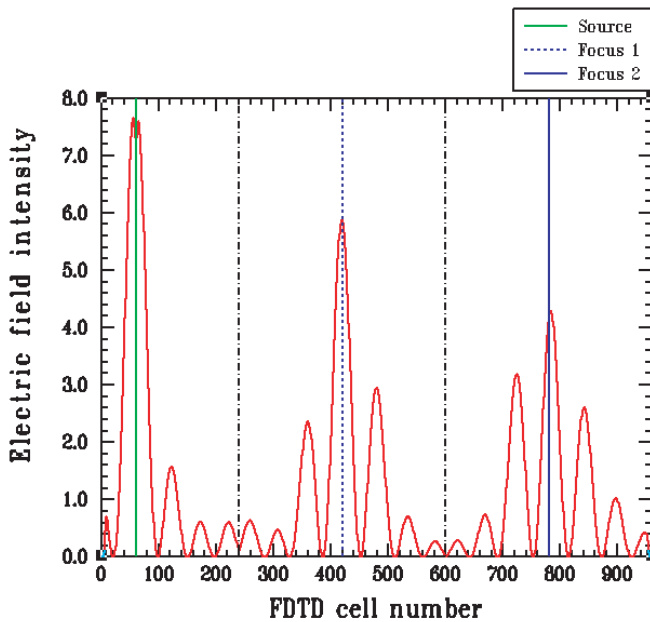
To emphasize the beam dynamics further, the electric field intensity distribution for a case for which the source is far from the slab is given in Figure 1.14*a*. The line source is 180 cells in front of a 360-cell-deep lossy Drude slab with  $n_{\text{real}}(\omega_0) \cong -1$  and  $\Gamma = 10^{-5}\omega_0$ . The paraxial focusing of the beam within the slab and external to it is readily apparent. The waists of the beam within the slab and beyond it occur at the predicted locations of the point foci. The longitudinal profile of the intensity along the beam axis is given in Figure 1.14*b*. The location of the beam foci coincide with the locations of the predicted point foci. These results correlate nicely to those shown in [42] for the corresponding lossy Lorentz slab.

The use of a planar DNG slab as a lens is illustrated with an FDTD simulation of the focusing of a Gaussian beam. A diverging CW-modulated Gaussian beam is assumed to be normally incident on such a planar DNG slab  $n_{\text{real}}(\omega_0) \approx -1$ . The waist of the beam was  $\lambda_0/2$  at the total field–scattered field plane from which it was launched into the simulation space. This source plane was  $2\lambda_0$  away from the DNG interface so that there would be sufficient distance for the beam to diverge before it hit the interface. The DNG slab also had a depth of  $2\lambda_0$ . Thus the locations of the foci are degenerate at  $z_{f1} = |z_0| = 2\lambda_0$  and  $z_{f2} = 2d - |z_0| = 2\lambda_0$ , which occur at the back face of the slab. The waist of the beam at this focus should be approximately the same as it is in the source plane. This behavior is illustrated in Figure 1.15. This result clearly shows that the planar DNG medium turns the diverging wave vectors toward the beam axis and, hence, acts as a lens to focus the beam. Since all angles of refraction are the negative of their angles of incidence for the  $n_{\text{real}}(\omega_0) \approx -1$  slab, the initial beam distribution is essentially recovered at the back face of the slab; that is, as designed, the focal plane of the beam in the DNG medium is located at the back face of the DNG slab. From the electric field intensity obtained from the FDTD simulation, we note that the peak intensity is about 18 percent lower than its value at the original waist of the Gaussian beam. This variance stems from the presence of additional wave processes, such as surface wave generation, and from dispersion and loss in the actual Drude model used to define the DNG slab in the FDTD simulation.

The corresponding results for the Gaussian beam interacting with the matched DNG slab with  $n_{\text{real}}(\omega_0) \approx -6$  reveals related but different results. In contrast to the  $n_{\text{real}}(\omega_0) \approx -1$  case, when the beam interacts with the matched DNG slab with  $n_{\text{real}}(\omega_0) \approx -6$ , there is little focusing observed. The negative angles of refraction dictated by Snell's law are shallower for this higher magnitude of the refractive index, that is,  $\theta_{\text{trans}} \approx -\sin^{-1}[\sin(\theta_{\text{inc}})/6]$ . Rather than a strong focusing, the medium channels power from the wings of the beam toward its axis, hence maintaining its amplitude as it propagates into the DNG medium. This difference in behaviors between the two types of DNG slabs is illustrated in Figure 1.16. A Gaussian beam is launched from a source plane which is  $2\lambda_0$  from the front of a pair of DNG slabs. Each slab is  $\lambda_0$  deep. The first DNG slab has  $n_{\text{real}}(\omega_0) \approx -1$  and the second has  $n_{\text{real}}(\omega_0) \approx -6$ , both having  $\Gamma = 10^{-5}\omega_0$ .



(a)



(b)

**Figure 1.14** (a) The FDTD predicted electric field intensity distribution illustrates the focusing of the field generated by a line source in a  $n_{\text{real}}(\omega_0) \approx -1$  DNG slab. (b) Longitudinal profile of electric field intensity distribution. The actual beam foci coincide with the predicted locations of the point foci.

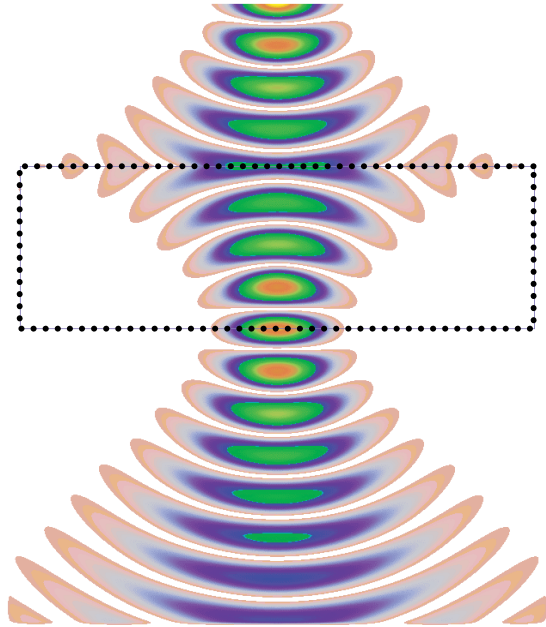
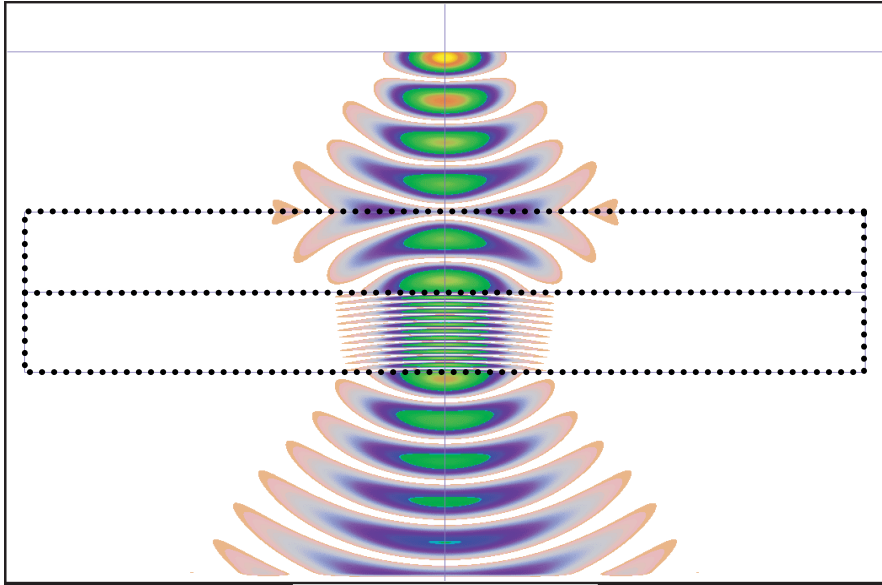


**Figure 1.15** The FDTD predicted electric field intensity distribution illustrates the focusing of a diverging Gaussian beam with a  $n_{\text{real}}(\omega_0) \approx -1$  DNG slab. The source and slab distances were selected to have the DNG slab focus the beam at its output face. From [22]. Copyright © 2003 by the Optical Society of America.

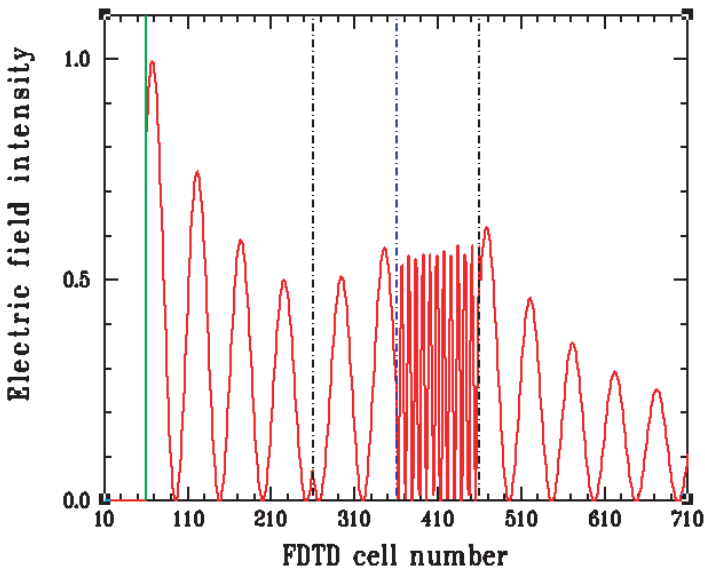
The FDTD predicted electric field intensity distribution given in Figure 1.16a shows the beam is initially focused by the  $n_{\text{real}}(\omega_0) \approx -1$  slab, as expected. The  $n_{\text{real}}(\omega_0) \approx -6$  slab then channels the beam through it with only minor focusing. The strong axial compression of the beam caused by the (factor of 6) decrease in the wavelength in the  $n_{\text{real}}(\omega_0) \approx -6$  slab is apparent. The longitudinal profile of the electric field intensity along the beam axis is shown in Figure 1.16b. It shows the field is being focused throughout both slabs and the slab pair produces an output intensity that is larger than its input value.

We note that in all of the focusing cases considered the beam appears to diverge significantly once it leaves the DNG slab. The properties of the DNG medium hold the beam together as it propagates through the slab. Once it leaves the DNG slab, the beam must begin diverging; that is, if the DNG slab focuses the beam as it enters, the same physics will cause the beam to diverge as it exits. Moreover, there will be no focusing of the power from the wings to maintain the center portion of the beam. The rate of divergence of the exiting beam will be determined by its original value and the properties and size of the DNG medium. We also point out that a beam focused into a DNG slab will generate a diverging beam within the slab and a converging beam upon exit from the slab. This behavior has also been confirmed with the FDTD simulator.

It must be mentioned that a planar DNG slab is unable to focus a collimated beam (i.e., flat beam) or a plane wave, since the negative angle of refraction can occur only if there is oblique incidence. To focus a flat Gaussian beam (one with nearly an infinite radius of curvature), one must resort to a curved lens. In contrast to focusing (diverging) a plane wave with a convex (concave) DPS lens,

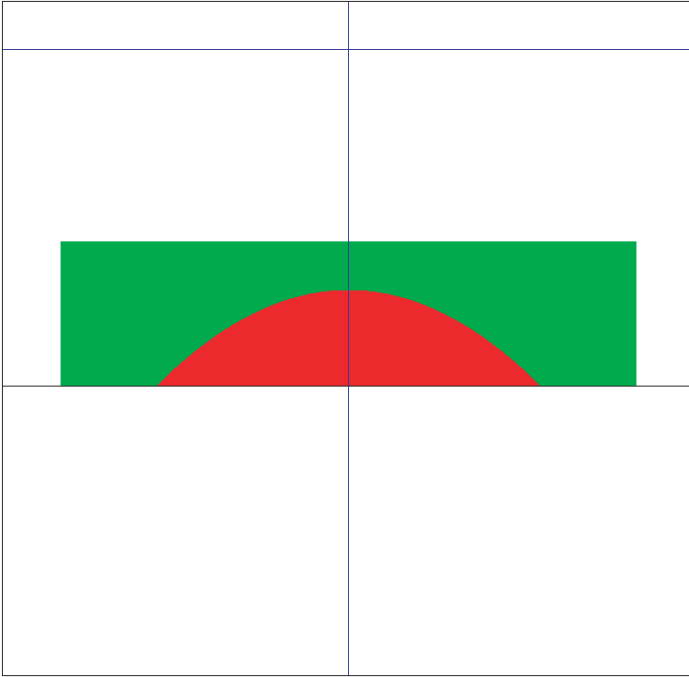


(a)

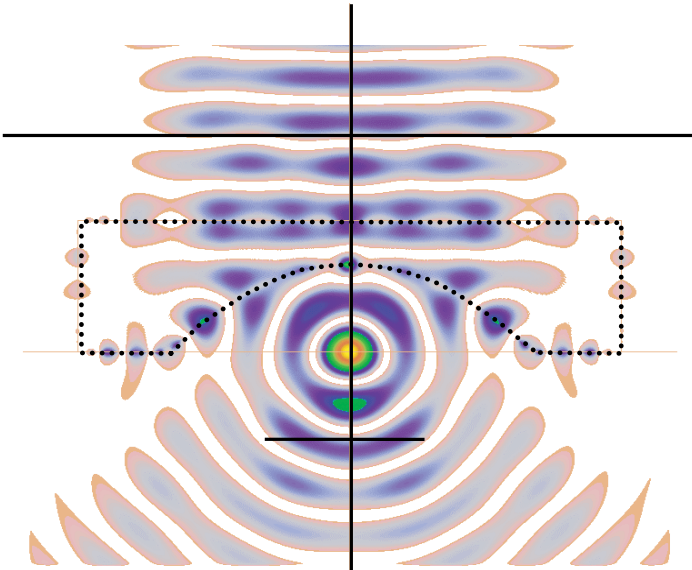


(b)

**Figure 1.16** (a) The FDTD predicted electric field intensity distribution illustrates the focusing of a Gaussian beam in the first  $n_{\text{real}}(\omega_0) \approx -1$  DNG slab and the channeling of the resulting beam in the second  $n_{\text{real}}(\omega_0) \approx -6$  DNG slab. (b) Longitudinal profile of electric field intensity distribution. The slab pair focuses the beam and produces an output amplitude which is expectedly larger than its input value.



(a)



(b)

**Figure 1.17** (a) Planoconcave DNG lens configuration. (b) The FDTD predicted electric field intensity distribution illustrates the focusing of a Gaussian beam with the planoconcave lens. The focal spot has both the longitudinal ( $0.19\lambda_0$ ) and transverse ( $0.17\lambda_0$ ) dimensions approximately equal.

one must use a concave (convex) DNG lens to achieve a focus (divergence). Such a planoconcave DNG lens with  $n_{\text{real}}(\omega_0) \approx -1$  is shown in Figure 1.17a. It was formed by removing a parabolic section from the back side of a slab that was  $1.5\lambda_0$  deep and  $6.0\lambda_0$  wide. The focal length was chosen to be  $\lambda_0$ , and the location of the focus was chosen to be at the center of the back face of the slab. The full width of the removed parabolic section at the back face was  $4\lambda_0$ . A Gaussian beam with a waist of  $2\lambda_0$  was launched  $2\lambda_0$  distance away from the planar side of this lens and was normally incident on it. It is known that a DPS planoconvex lens of index  $n_{\text{DPS}}$  with a similar radius of curvature  $R = 2\lambda_0$  (the red region in Fig. 1.17a) would have a focus located a distance  $f_{\text{DPS}} = R/(n_{\text{DPS}} - 1) = 2\lambda_0/(n_{\text{DPS}} - 1)$  from its back face. Thus, to have the focal point within the very near field, as it is in the DNG case, the index of refraction would have to be very large. In fact, to have it located at the back face would require  $n_{\text{DPS}} \rightarrow \infty$ . This would also mean that very little of the incident beam would be transmitted through such a high-index lens because the magnitude of the reflection coefficient would approach 1. In contrast, the DNG lens achieves a greater bending of the incident waves with only moderate absolute values of the refractive index and is impedance matched to the incident medium. Moreover, since the incident beam waist occurs at the lens, the expected waist of the focused beam would be  $w_{\text{focus}} \approx (\lambda_0 f_{\text{DPS}})/(\pi w_0) = \lambda_0/[\pi(n_{\text{DPS}} - 1)]$  [55]. For a normal glass lens  $n_{\text{DPS}} \approx 1.5$ ; hence, the transverse waist at the focus would be  $w_{\text{focus}} \approx \lambda_0/1.57$  and the corresponding intensity half-maximum waist would be  $0.589w_{\text{focus}}$ . The longitudinal size of the focus is the depth of focus, which for the normal glass lens would be  $2(\pi w_{\text{focus}}^2/\lambda_0)$ . Again, to achieve a focus that is significantly subwavelength using a DPS lens, a very large index value would be required and would lead to similar disadvantages in comparison to the DNG lens. However, for the DNG planoconcave lens, one obtains more favorable results. Figure 1.17b shows a snapshot of the FDTD-predicted electric field intensity distribution when the intensity is peaked at the focal point. The radius of the focus along the beam axis (half-intensity radius) is measured to be about  $\lambda_0/5$  and along the transverse direction it is about  $\lambda_0/6$ . This subwavelength focal region is significantly smaller than would be expected from the corresponding, traditional DPS lens. Moreover, even though the focal point is in the extreme near field of the lens, the focal region is nearly symmetrical and has a resolution that is much smaller than a wavelength.

## 1.11 METAMATERIALS WITH A ZERO INDEX OF REFRACTION

Metamaterials, in which the permittivity and/or permeability are near zero and thus the refractive index is much smaller than unity, can offer exciting potential applications. Their location on the  $\varepsilon - \mu$  space diagram is represented by the red dot in Figure 1.18. Planar metamaterials that exhibit both positive and negative values of the index of refraction near zero have been realized experimentally by several research groups [8, 31, 32, 56–62] and are discussed in several chapters

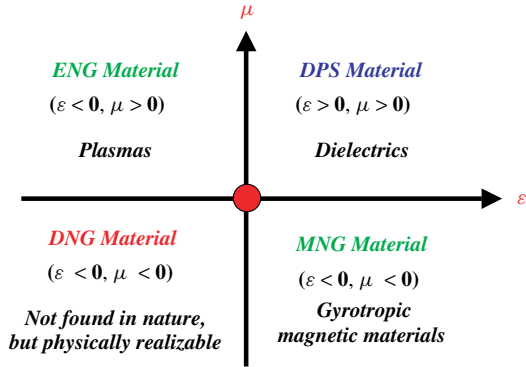


**Figure 1.18** The zero-index media lie at the intersection of the various types of materials.

of this book. Within these studies, there have also been several demonstrations, both theoretically and experimentally, of planar metamaterials that exhibit a zero index of refraction within a specified frequency band. In particular, by matching the resonances in a series–parallel lumped-element circuit realization of a DNG metamaterial at a specified frequency, the propagation constant as a function of frequency continuously passes through zero (giving a zero index) with a nonzero slope (giving a nonzero group speed) in its transition from a DNG region of its operational behavior to a DPS region [56, 59, 63]. Several applications of these series–parallel metamaterials have been proposed and realized (e.g., phase shifters, couplers, and compact resonators).

Several investigations have also presented volumetric metamaterials that exhibit near-zero-index medium properties, for instance [64–68]. These zero-index electromagnetic bandgap (EBG) structure studies include working in a passband. By introducing a source into a zero-index EBG with an excitation frequency that lies within the EBG’s passband, Enoch, Tayeb, and co-workers produced extremely narrow antenna patterns [66–68, Chapter 10]. Alù et al. have also shown theoretically that, by covering a subwavelength tiny aperture in a flat perfectly conducting screen with a slab of materials with  $\mu \ll \mu_o$ , one can significantly increase the power transmitted through such a hole, due to the coupling of the incident wave into the leaky wave supported by such a layer [69]. By covering both sides of the hole, not only can one increase the transmitted power through the hole but this power can be directed as a sharp beam in a given direction [69, 70].

These results stimulated a study by Ziolkowski [71] that details the propagation and scattering properties of a passive, dispersive metamaterial that is matched to free space and has an index of refraction equal to zero. One-, two-, and three-dimensional problems corresponding to source and scattering configurations have been treated analytically. The 1D and 2D results have been confirmed numerically with FDTD simulations. It has been shown that the electromagnetic fields in a matched zero-index medium [i.e.,  $\epsilon_{\text{real}}(\omega_0) \cong 0$ ,  $\mu_{\text{real}}(\omega_0) \cong 0$  so that  $Z(\omega_0) = Z_0$  and  $n_{\text{real}}(\omega_0) \cong 0$ ] take on a static character in space, yet remain dynamic in time, in such a manner that the underlying physics remains associated with propagating fields.

To illustrate this behavior, consider Maxwell's equations:

$$\begin{aligned}\nabla \times \mathbf{E}_\omega &= -j\omega\mu\mathbf{H}_\omega & \nabla \cdot (\varepsilon\mathbf{E}_\omega) &= \rho_\omega \\ \nabla \times \mathbf{H}_\omega &= j\omega\varepsilon\mathbf{E}_\omega + \mathbf{J}_\omega & \nabla \cdot (\mu\mathbf{H}_\omega) &= 0\end{aligned}\quad (1.28)$$

When  $\varepsilon_{\text{real}}(\omega_0) \cong 0$  and  $\mu_{\text{real}}(\omega_0) \cong 0$ , Maxwell's equations reduce to

$$\begin{aligned}\nabla \times \mathbf{E}_\omega &= 0 & \nabla \cdot (\varepsilon\mathbf{E}_\omega) &= 0 \\ \nabla \times \mathbf{H}_\omega &= \vec{J}_\omega & \nabla \cdot (\mu\mathbf{H}_\omega) &= 0\end{aligned}\quad (1.29)$$

The equations on the right are automatically satisfied in the zero-index medium if the fields are finite. Thus one obtains staticlike equations for the fields within a zero-index medium. For an infinite cylindrical zero-index medium surrounded by free space, the solutions for a infinite line current

$$\mathbf{J}_\omega(\rho, \phi, z) = I_0 \frac{\delta(\rho)}{2\pi\rho} \hat{z} \quad (1.30)$$

are

$$\begin{aligned}\mathbf{E}_\omega(\rho, \phi, z) &= -Z_0 \frac{I_0}{2\pi a} \frac{jH_0^{(2)}(k_0 a)}{H_1^{(2)}(k_0 a)} \hat{z} \\ \mathbf{H}_\omega(\rho, \phi, z) &= \frac{I_0}{2\pi\rho} \hat{\phi}\end{aligned}\quad (1.31)$$

for  $r \leq a$  and

$$\begin{aligned}\mathbf{E}_\omega(\rho, \phi, z) &= -Z_0 \frac{I_0}{2\pi a} \frac{jH_0^{(2)}(k_0\rho)}{H_1^{(2)}(k_0 a)} \hat{z} \\ \mathbf{H}_\omega(\rho, \phi, z) &= \frac{I_0}{2\pi a} \frac{H_1^{(2)}(k_0\rho)}{H_1^{(2)}(k_0 a)} \hat{\phi}\end{aligned}\quad (1.32)$$

for  $r > a$ , where  $k_0 = \omega\sqrt{\varepsilon_0}\sqrt{\mu_0}$ . Thus the solution inside the cylinder has a spatially constant electric field and magnetostatic magnetic field, whereas outside the cylinder, cylindrical waves propagate away from the source. Nonetheless, there is power flowing outward from the source in both regions; that is, the time-averaged Poynting's vector is

$$\langle \mathbf{S}_\omega \rangle = \frac{Z_0 I_0^2}{(2\pi a)^2} \frac{1}{|H_1^{(2)}(k_0 a)|^2} \frac{2}{\pi k_0 \rho} \hat{\rho} \quad (1.33)$$

If the spectrum of the time history driving the source is localized, one can easily take into account the time variations of the fields. In particular, one can approximately write

$$\begin{aligned}\mathbf{H}(\rho, \phi, z, t) &= \frac{I_0}{2\pi\rho} f(t) \hat{\phi} \\ \mathbf{E}(\rho, \phi, z, t) &\approx -Z_0 \frac{I_0}{2\pi a} f(t) \hat{z}\end{aligned}\quad (1.34)$$

These 2D results have been confirmed with FDTD simulations. The FDTD predicted electric field distributions at various times are shown in Figure 1.19

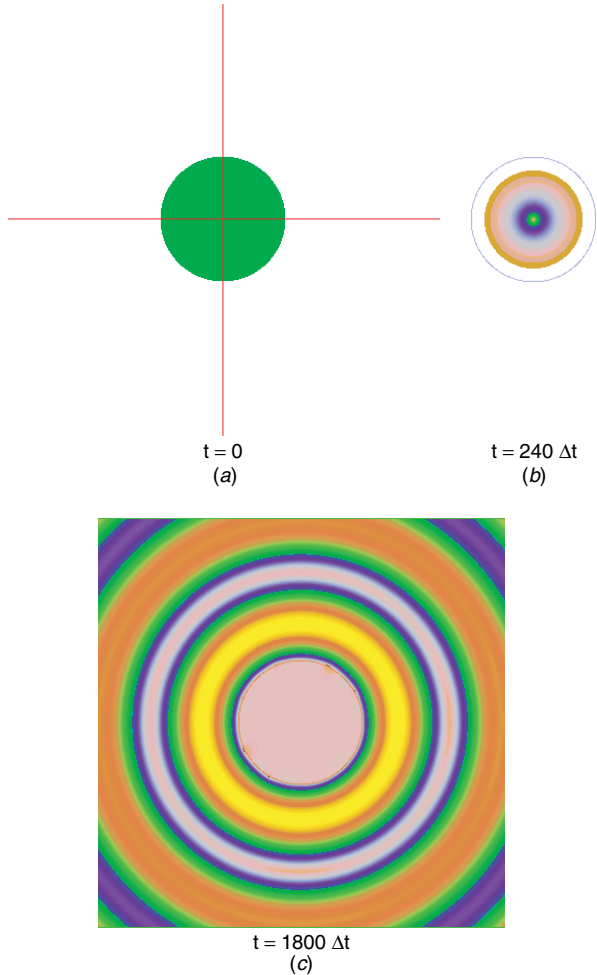
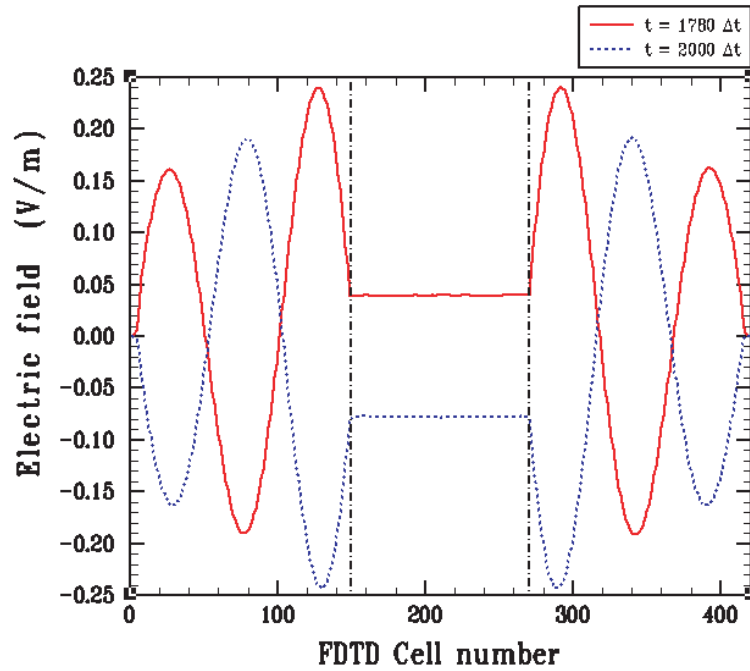
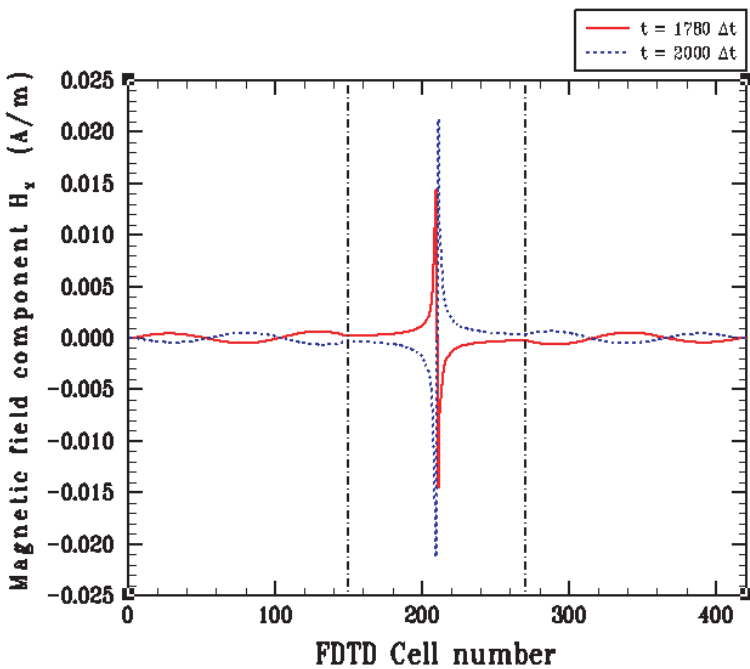


**Figure 1.19** An infinite line source is located at the center of a matched zero-index infinite cylinder. The FDTD predicted electric field intensity distributions are shown for (a)  $t = 0$ , (b)  $t = 240\Delta t$ , and (c)  $1800\Delta t$ . A cylindrical wave propagates away from the cylinder while a uniform electric field intensity develops within the cylinder. From [71]. Copyright © 2004 by the American Physical Society.

at the initial time, early in the simulation, and at the end of the simulation. The infinite line source is driven at 30 GHz, is orthogonal to the plane, and is centered in the zero-index cylinder, which had a  $0.6\lambda_0 = 60$ -cell radius. The time sequence shows that the electromagnetic field energy propagates radially outward through the zero-index cylinder into the free-space region. The cross-sectional profiles of the electric and magnetic field distributions are given in Figures 1.20a and b, respectively. The electric field is clearly spatially constant throughout the entire cylinder but varies in time. On the other hand, the magnetic field component within the cylinder has taken on the predicted magnetostatic spatial characteristics and also varies in time. The electromagnetic field within the matched zero-index cylinder transitions to an oscillatory, propagating field once it exits the cylinder and enters free space. Comparisons of the time histories at various locations



(a)



(b)

**Figure 1.20** Cross-sectional profiles of (a) electric field and (b) magnetic field when a line source is driven at the center of a zero-index cylinder. From [71]. Copyright © 2004 by the American Physical Society.

within the cylinder show that there is zero phase difference between any two points once steady state has been achieved.

There have been related discussions [72–74] of metamaterials that exhibit “nihility,” basically the zero-index properties described here. The generalization to more general bianisotropic media in which only the chiral parameters are nonzero has been considered in [74]. The latter suggests the intriguing possibility of force-free *electromagnetic* field configurations in metamaterials exhibiting such chiral nihility. Force-free magnetic fields are used, for example, to explain the behavior of plasmas associated with solar prominences and spheromaks (toroidal plasma states). All of these zero-index medium examples simply further illustrate how “exotic” the physical properties of metamaterials can be.

## 1.12 SUMMARY

---

In this chapter, we briefly reviewed the history and several selected topics associated with the fundamental properties of DNG metamaterials. We have shown how wave interaction with such materials can lead to interesting, unconventional features not observed in standard DPS media. A more comprehensive review can be found in our recent paper [48]. These physics characteristics can lead to exciting engineering concepts with future potential applications. Some of these concepts will be reviewed in Chapter 2.

## REFERENCES

---

1. J. C. Bose, “On the rotation of plane of polarisation of electric waves by a twisted structure,” *Proc. Roy. Soc.*, vol. 63, pp. 146–152, 1898.
2. I. V. Lindell, A. H. Sihvola, and J. Kurkijarvi, “Karl F. Lindman: The last Hertzian, and a Harbinger of electromagnetic chirality,” *IEEE Antennas Propag. Mag.*, vol. 34, no. 3, pp. 24–30, 1992.
3. W. E. Kock, “Metallic delay lenses,” *Bell Sys. Tech. J.*, vol. 27, pp. 58–82, 1948.
4. V. G. Veselago, “The electrodynamics of substances with simultaneously negative values of  $\epsilon$  and  $\mu$ ,” *Sov. Phys. Uspekhi*, vol. 10, no. 4, pp. 509–514, 1968. [*Usp. Fiz. Nauk*, vol. 92, pp. 517–526, 1967.]
5. D. R. Smith, W. J. Padilla, D. C. Vier, S. C. Nemat-Nasser, and S. Schultz, “Composite medium with simultaneously negative permeability and permittivity,” *Phys. Rev. Lett.*, vol. 84, no. 18, pp. 4184–4187, May 2000.
6. R. A. Shelby, D. R. Smith, and S. Schultz, “Experimental verification of a negative index of refraction,” *Science*, vol. 292, no. 5514, pp. 77–79, 6 Apr. 2001.
7. J. B. Pendry, “Negative refraction makes a perfect lens,” *Phys. Rev. Lett.*, vol. 85, no. 18, pp. 3966–3969, Oct. 2000.
8. C. Caloz, C.-C. Chang, and T. Itoh, “Full-wave verification of the fundamental properties of left-handed materials in waveguide configurations,” *J. Appl. Phys.*, vol. 90, no. 11, pp. 5483–5486, Dec. 2001.
9. A. K. Iyer and G. V. Eleftheriades, “Negative refractive index metamaterials supporting 2-D waves,” in *2002 IEEE MTT International Microwave Symposium (IMS) Digest*, Seattle, WA, June 2–7, 2002, pp. 1067–1070.
10. C. Caloz, H. Okabe, T. Iwai, T. Itoh, “Transmission line approach of left-handed materials,” paper presented at the 2002 IEEE AP-S International Symposium and USNC/URSI

- National Radio Science Meeting, San Antonio, TX, June 16–21, 2002, abstract, *URSI Digest*, p. 39.
11. I. V. Lindell, S. A. Tretyakov, K. I. Nikoskinen, and S. Ilvonen, “BW media—Media with negative parameters, capable of supporting backward waves,” *Microwave Opt. Tech. Lett.*, vol. 31, no. 2, pp. 129–133, Oct. 2001.
  12. R. W. Ziolkowski and E. Heyman, “Wave propagation in media having negative permittivity and permeability,” *Phys. Rev. E*, vol. 64, no. 5, 056625, Oct. 2001.
  13. R. W. Ziolkowski and F. Auzanneau, “Passive artificial molecule realizations of dielectric materials,” *J. Appl. Phys.*, vol. 82, no. 7, pp. 3195–3198, Oct. 1997.
  14. F. Auzanneau and R. W. Ziolkowski, “Microwave signal rectification using artificial composite materials composed of diode loaded, electrically small dipole antennas,” *IEEE Trans. Microwave Theory Tech.*, vol. 46, no. 11, pp. 1628–1637, Nov. 1998.
  15. D. C. Wittwer and R. W. Ziolkowski, “Two time-derivative Lorentz material (2TDLM) formulation of a Maxwellian absorbing layer matched to a lossy media,” *IEEE Trans. Antennas Propag.*, vol. 48, no. 2, pp. 192–199, Feb. 2000.
  16. R. W. Ziolkowski, “Superluminal transmission of information through an electromagnetic metamaterial,” *Phys. Rev. E*, vol. 63, 046604, Apr. 2001.
  17. R. W. Ziolkowski and C.-Y. Cheng, “Existence and design of trans-vacuum-speed metamaterials,” *Phys. Rev. E*, vol. 68, 026612, Aug. 2003.
  18. D. R. Smith and N. Kroll, “Negative refractive index in left-handed materials,” *Phys. Rev. Lett.*, vol. 85, pp. 2933–2936, Oct. 2000.
  19. N. Engheta, “An idea for thin subwavelength cavity resonators using metamaterials with negative permittivity and permeability,” *IEEE Antennas Wireless Propag. Lett.*, vol. 1, pp. 10–13, 2002.
  20. J. A. Kong, B.-I. Wu, and Y. Zhang, “A unique lateral displacement of a Gaussian beam transmitted through a slab with negative permittivity and permeability,” *Microwave Opt. Tech. Lett.*, vol. 33, pp. 136–139, Mar. 2002.
  21. P. Kolinko and D. R. Smith, “Numerical study of electromagnetic waves interacting with negative index materials,” *Opt. Express*, vol. 11, pp. 640–648, Apr. 2003.
  22. R. W. Ziolkowski, “Pulsed and CW Gaussian beam interactions with double negative metamaterial slabs,” *Opt. Express*, vol. 11, pp. 662–681, Apr. 2003.
  23. R. W. Ziolkowski, “Pulsed and CW Gaussian beam interactions with double negative metamaterial slabs: Errata,” *Opt. Express*, vol. 11, no. 13, pp. 1596–1597, June 2003.
  24. S. Foteinopoulou, E. N. Economou, and C. M. Soukoulis, “Refraction in media with a negative refractive index,” *Phys. Rev. Lett.*, vol. 90, 107402, Mar. 2003.
  25. A. Alù, and N. Engheta, “Guided modes in a waveguide filled with a pair of single-negative (SNG), double-negative (DNG), and/or double-positive (DPS) layers,” *IEEE Trans. Microwave Theory Tech.*, vol. MTT-52, no. 1, pp. 199–210, Jan. 2004.
  26. A. Alù and N. Engheta, “An overview of salient properties of guided-wave structures with double-negative and single-negative metamaterials,” in *Negative Refraction Metamaterials: Fundamental Properties and Applications* (G. V. Eleftheriades and K. G. Balmain, Eds.), IEEE Press/Wiley, Hoboken, NJ, 2005, Chap. 15, pp. 339–380.
  27. N. Engheta, “Ideas for potential applications of metamaterials with negative permittivity and permeability,” *Advances in Electromagnetics of Complex Media and Metamaterials*, NATO Science Series (S. Zouhdi, A. H. Sihvola, and M. Arsalane, Eds.), Kluwer Academic, Dordrecht, The Netherlands, 2002, pp. 19–37.
  28. I. S. Nefedov and S. A. Tretyakov, “Waveguide containing a backward-wave slab,” e-print in arXiv:cond-mat/0211185 v1, at <http://arxiv.org/pdf/cond-mat/0211185>, Nov. 10, 2002.
  29. B.-I. Wu, T. M. Grzegorzczuk, Y. Zhang, and J. A. Kong, “Guided modes with imaginary transverse wave number in a slab waveguide with negative permittivity and permeability,” *J. Appl. Phys.*, vol. 93, no. 11, pp. 9386–9388, June 2003.
  30. A. Topa, “Contradirectional interaction in a NRD waveguide coupler with a metamaterial slab,” paper presented at XXVII General Assembly of International Union of Radio Science (URSI GA’02), Maastricht, The Netherlands, Aug. 17–24, 2002, *CD Digest*, paper no. 1878.

31. A. Grbic and G. V. Eleftheriades, "Overcoming the diffraction limit with a planar left-handed transmission line lens," *Phys. Rev. Lett.*, vol. 92, no. 11, 117403, Mar. 2004.
32. A. A. Grbic and G. V. Eleftheriades, "Experimental verification of backward-wave radiation from a negative refractive index metamaterial," *J. Appl. Phys.*, vol. 92, pp. 5930–5935, Nov. 2002.
33. J. Lu, T. M. Grzegorzczak, Y. Zhang, J. Pacheco, Jr., B.-I. Wu, J. A. Kong, and M. Chen, "Čerenkov radiation in materials with negative permittivity and permeability," *Opt. Express*, vol. 11, pp. 723–734, Apr. 2003.
34. Z. M. Zhang and C. J. Fu, "Unusual photon tunneling in the presence of a layer with negative refractive index," *Appl. Phys. Lett.*, vol. 80, pp. 1097–1099, Feb. 2002.
35. L. Wu, S. He, and L. Chen, "On unusual narrow transmission bands for a multi-layered periodic structure containing left-handed materials," *Opt. Express*, vol. 11, pp. 1283–1290, June 2003.
36. R. W. Ziolkowski and A. Kipple, "Application of double negative metamaterials to increase the power radiated by electrically small antennas," *IEEE Trans. Antennas Propag.*, vol. 51, no. 10, pp. 2626–2640, Oct. 2003.
37. R. W. Ziolkowski, "Gaussian beam interactions with double negative (DNG) metamaterials," in *Negative Refraction Metamaterials: Fundamental Properties and Applications* (G. V. Eleftheriades and K. G. Balmain, Eds.), IEEE Press/Wiley, Hoboken, NJ, 2005, Chapter 4, pp. 171–211.
38. A. Taflov, *Computational Electrodynamics: The Finite-Difference Time-Domain Method*, Artech House, Norwood, MA, 1995.
39. D. C. Wittwer and R. W. Ziolkowski, "Maxwellian material based absorbing boundary conditions for lossy media in 3D," *IEEE Trans. Antennas Propag.*, vol. 48, pp. 200–213, Feb. 2000.
40. R. A. Shelby, D. R. Smith, S. C. Nemat-Nasser, and S. Schultz, "Microwave transmission through a two-dimensional, isotropic, left-handed metamaterial," *Appl. Phys. Lett.*, vol. 78, pp. 489–491, Jan. 2000.
41. M. M. I. Saadoun, and N. Engheta, "Theoretical study of electromagnetic properties of non-local omega media" in *Progress in Electromagnetic Research (PIER) Monograph Series*, Vol. 9 (A. Priou, Guest Ed.), EMW Publishing, Cambridge, MA, 1994, Chapter 15, pp. 351–397.
42. P. F. Loschialpo, D. L. Smith, D. W. Forester, and F. J. Rachford, "Electromagnetic waves focused by a negative-index planar lens," *Phys. Rev. E*, vol. 67, 025602(R), Feb. 2003.
43. M. K. Kärkkäinen, "Numerical study of wave propagation in uniaxially anisotropic Lorentzian backward-wave slabs," *Phys. Rev. E*, vol. 68, 026602, Aug. 2003.
44. R. W. Ziolkowski and A. Kipple, "Causality and double-negative metamaterials," *Phys. Rev. E*, vol. 68, 026615, Aug. 2003.
45. A. Alù, and N. Engheta, "Pairing an epsilon-negative slab with a mu-negative slab: Anomalous tunneling and transparency," *IEEE Trans. Antennas Propag.*, *Special Issue on Metamaterials*, vol. AP-51, no. 10, pp. 2558–2570, Oct. 2003.
46. A. Alù and N. Engheta, "A physical insight into the 'growing' evanescent fields of double-negative metamaterial lens using its circuit equivalence," *IEEE Trans. Antennas Propag.*, vol. 54, pp. 268–272, Jan. 2006.
47. A. Alù and N. Engheta, "Radiation from a traveling-wave current sheet at the interface between a conventional material and a material with negative permittivity and permeability," *Microwave Opt. Tech. Lett.*, vol. 35, no. 6, pp. 460–463, Dec. 2002.
48. N. Engheta and R. W. Ziolkowski, "A positive future for double-negative metamaterials," *IEEE Trans. Microwave Theory Tech.*, *Special Issue on Metamaterial Structures, Phenomena, and Applications*, vol. 53, no. 4 (part II), pp. 1535–1556, Apr. 2005.
49. C.-Y. Cheng and R. W. Ziolkowski, "Tailoring double negative metamaterial responses to achieve anomalous propagation effects along microstrip transmission line," *IEEE Trans. Microwave Theory Tech.*, vol. 51, pp. 2306–2314, Dec. 2003.
50. F. Gardiol, *Microstrip Circuits*, Wiley, New York, 1994, pp. 48–50.

51. W. J. Getsinger, "Microstrip dispersion model," *IEEE Trans. Microwave Theory Tech.*, vol. MTT-21, pp. 34–39, Jan. 1973.
52. D. R. Smith, D. Schurig, M. Rosenbluth, S. Schultz, S. Anantha Ramakrishna, and J. B. Pendry, "Limitation on subdiffraction imaging with a negative refractive index slab," *Appl. Phys. Lett.*, vol. 82, no. 10, pp. 1506–1508, Mar. 2003.
53. C. Luo, S. G. Johnson, and J. D. Joannopoulos, "Subwavelength imaging in photonic crystals," *Phys. Rev. B*, vol. 68, 045115, July 2003.
54. A. Alù and N. Engheta, "Tunneling and 'growing evanescent envelopes' in a pair of cascaded sets of frequency selective surfaces in their band gaps," in *Proceedings of the 2004 URSI International Symposium on Electromagnetic Theory*, vol. 1, Pisa, Italy, May 24–27, 2004, pp. 90–92.
55. B. E. A. Saleh and M. C. Teich, *Fundamentals of Photonics*, Wiley, New York, 1991, pp. 94–95.
56. C. Caloz and T. Itoh, "Microwave applications of novel metamaterials," in *Proceedings of the International Conference on Electromagnetics in Advanced Applications, ICEAA'03*, Torino, Italy, Sept. 2003, pp. 427–430.
57. C. Caloz, A. Sanada, and T. Itoh, "A novel composite right/left-handed coupled-line directional coupler with arbitrary coupling level and broad bandwidth," *IEEE Trans. Microwave Theory Tech.*, vol. 52, pp. 980–992, Mar. 2004.
58. C. Caloz and T. Itoh, "A novel mixed conventional microstrip and composite right/left-handed backward wave directional coupler with broadband and tight coupling characteristics," *IEEE Microwave Wireless Components Lett.*, vol. 14, no. 1, p. 31–33, Jan. 2004.
59. G. G. V. Eleftheriades, A. K. Iyer, and P. C. Kremer, "Planar negative refractive index media using periodically  $L$ - $C$  loaded transmission lines," *IEEE Trans. Microwave Theory Tech.*, vol. 50, pp. 2702–2712, Dec. 2002.
60. R. Islam, F. Eleck, and G. V. Eleftheriades, "Coupled-line metamaterial coupler having co-directional phase but contra-directional power flow," *Electron. Lett.*, vol. 40, no. 5, pp. 315–317, Mar. 2004.
61. A. A. Oliner, "A periodic-structure negative-refractive-index medium without resonant elements," paper presented at 2002 IEEE AP-S Int. Symp./USNC/URSI National Radio Science Meeting, San Antonio, TX, June 16–21, 2002, *URSI Digest*, p. 41.
62. A. A. Oliner, "A planar negative-refractive-index medium without resonant elements," in *MTT Int. Microwave Symp. (IMS'03) Digest*, Philadelphia, PA, June 8–13, 2003, pp. 191–194.
63. R. W. Ziolkowski and C.-Y. Cheng, "Lumped element models of double negative metamaterial-based transmission lines," *Radio Sci.*, vol. 39, RS2017, doi: 10.1029/2003RS002995, Apr. 2004.
64. B. Gralak, S. Enoch, and G. Tayeb, "Anomalous refractive properties of photonic crystals," *J. Opt. Soc. Am. A*, vol. 17, no. 6, pp. 1012–1020, June 2000.
65. M. Notomi, "Theory of light propagation in strongly modulated photonic crystals: Refractionlike behavior in the vicinity of the photonic bandgap," *Phys. Rev. B*, vol. 62, no. 16, 10696, Oct. 2000.
66. S. Enoch, G. Tayeb, P. Sabouroux, N. Guerin, and P. Vincent, "A metamaterial for directive emission," *Phys. Rev. Lett.*, vol. 89, 213902, Nov. 2002.
67. S. Enoch, G. Tayeb, and B. Gralak, "The richness of dispersion relation of electromagnetic bandgap materials," *IEEE Trans. Antennas Propag.*, vol. 51, no. 10, pp. 2659–2666, Oct. 2003.
68. G. Tayeb, S. Enoch, P. Vincent, and P. Sabouroux, "A compact directive antenna using ultrarefractive properties of metamaterials," in *Proceedings of the International Conference on Electromagnetics in Advanced Applications, ICEAA'03*, Torino, Italy, Sept. 2003, pp. 423–426.
69. A. Alù, F. Bilotti, N. Engheta, and L. Vegni, "How metamaterials may significantly affect the wave transmission through a sub-wavelength hole in a flat perfectly conducting

- screen,” paper present at Workshop on Metamaterials for Microwave and (Sub) millimetre Wave Applications: Photonic Bandgap and Double Negative Designs, Components and Experiments, London, Nov. 24, 2003.
70. A. Alù, F. Bilotti, N. Engheta, and L. Vegni, “Metamaterial bilayers for enhancement of wave transmission through a small hole in a flat perfectly conducting screen,” in *2004 IEEE Antennas and Propagation Society (AP-S) International Symposium Digest*, Monterey, CA, June 20–26, 2004, vol. 3, pp. 3163–3166.
  71. R. W. Ziolkowski, “Propagation in and scattering from a matched metamaterial having a zero index of refraction,” *Phys. Rev. E*, vol. 70, 046608, Oct. 2004.
  72. A. Lakhtakia, “On perfect lenses and nihility,” *Int. J. Infrared Millim. Waves*, vol. 23, no. 3, pp. 339–343, Mar. 2002.
  73. A. Lakhtakia, “An electromagnetic trinity from ‘negative permittivity’ and ‘negative permeability,’ ” *Int. J. Infrared Millim. Waves*, vol. 23, no. 6, pp. 813–818, June 2002.
  74. S. Tretyakov, I. Nefedov, A. Sihvola, S. Maslovski, and C. Simovski, “Waves and energy in chiral nihility,” *J. Electromagnetic Waves Appl.*, vol. 17, no. 5, pp. 695–706, May 2003.

